J. Fluid Mech. (2004), *vol.* 506, *pp.* 79–115.
DOI: 10.1017/S0022112004008481 Printed in the United Kingdom

Effect of surfactants on free-surface turbulent flows

By LIAN SHEN[1]†, DICK K. P. YUE[1] AND GEORGE S. TRIANTAFYLLOU[2]

[1]Department of Ocean Engineering, Massachusetts Institute of Technology, Cambridge, MA 02139, USA

[2]Department of Naval Architecture and Marine Engineering, National Technical University of Athens, Zografou 15773, Athens, Greece

(Received 17 December 2002 and in revised form 10 December 2003)

In two earlier papers, we studied the statistical and mechanistic structure of the turbulent boundary layer under a stress-free (clean) free surface. Findings there, such as the presence of inner and outer surface layers, are very much the direct result of the absence of shear stresses at the surface. The latter condition is easily lost when the surface is contaminated and surface elasticity varies with space and time. In this paper we consider the effect of surfactant on features of the free-surface turbulent flow. We perform direct numerical simulations of the Navier–Stokes equations subject to surfactant-laden free-surface boundary conditions for varying Reynolds and Marangoni numbers and low Froude numbers. As expected, the Marangoni effect decreases the horizontal turbulence intensity and normal vorticity at the surface. The direct effect on the turbulent kinetic energy is an increase in the dissipation and viscous diffusion and a decrease in the production near the surface relative to the clean case. The most prominent effect of the presence (of even a small amount) of surfactant is the drastic reduction in the surface divergence and the associated sharp decrease of up- and downwelling at the surface which has direct implications to near-surface turbulent transport. The observed surfactant effects on turbulent kinetic energy budget can be attributed to the generation of Marangoni vorticity at the free surface by approaching hairpin vortices. The Marangoni effect has also a direct effect on the boundary-layer structure, causing an increase of the thickness of the boundary layer and in the maxima of the mean shear near the surface. For moderate values of the Marangoni number, up-/downwelling effectively vanishes and the flow approaches a state independent of the Marangoni number. Guided by these results and to obtain theoretical insight, we develop a similarity solution for the mean flow. The analytic solution agrees well with the numerical data and provides precise measures for the multi-layer structure of the boundary layer. Based on the theoretical model, we derive scaling laws for the thickness of the inner and the outer boundary layers, which are also confirmed by numerical simulations.

1. Introduction

The turbulent boundary layer at a free surface plays an important role in the transfer of momentum, mass and heat across a gas–liquid interface. These are of direct

† Present address: Department of Civil Engineering, The Johns Hopkins University, Baltimore, MD 21218, USA.

importance in environmental and industrial applications, examples of which include the transfer of greenhouse gases between the atmosphere and the ocean, spreading of oil spills, remote sensing of ship wakes, and industrial processes involving gas–liquid flows. Despite this, our understanding of the fluid dynamics of free-surface turbulent boundary layers is still relatively limited.

Much existing work is based on the assumption of a clean free surface and vanishing shear stress at the surface. In natural waters, however, surface-active agents, i.e. surfactants (see Edwards, Brenner & Wasan 1991), are commonly present due to, for example, marine exudates and organic contaminants (Frew 1997; Hunter 1997). The presence of surfactants creates variations in the surface stresses which depend on concentration of the contaminant. The result is a closed-loop process (the Marangoni effect) wherein the concentration of surfactant is changed by the flow transport; the change in the surfactant concentration causes a variation of the surface tension, which in turn affects the fluid motion (see e.g. Sarpkaya 1996).

The ubiquitous presence of surfactants on nature waters and the significant effect of even small amounts of surfactants on the hydrodynamics have brought much attention to the problem of interactions between surfactants and underlying vortical and turbulent flows. Experimental investigations include Bernal *et al.* (1989) who showed that when vortex rings and vortex pairs move normal to a contaminated surface, generation of secondary and tertiary surface vorticities limit the outward motion of the vortex ring and force the vortex pair to rebound. Hirsa & Willmarth (1994) considered the interaction of a vortex pair with a surfactant surface and obtained detailed measurement of the flow field. The dynamics of vortex connection at a contaminated surface was studied experimentally by Gharib & Weigand (1996) for vortex rings and by Willert & Gharib (1997) for spatially modulated vortex pairs. Other laboratory measurements of surfactant effects include Anthony, Hirsa & Willmarth (1991) for a submerged turbulent jet, McKenna (2000) for an oscillating grid-stirred turbulence, and Flack, Saylor & Smith (2001) for turbulent flows beneath an air–water interface undergoing evaporative convection.

There are also numerical studies of surfactant-flow interactions (although somewhat more limited compared to experiments). Wang & Leighton (1990) and Tryggvason *et al.* (1992) considered the problem of a vortex pair approaching a surfactant surface for the zero-Froude-number case and qualitatively confirmed the observations of Bernal *et al.* (1989). Ananthakrishnan & Yeung (1994) investigated the effects of surfactants on surface waves generation by rising vorticity. They found that globally the free-surface deformation is damped, although locally short waves may be steepened. Tsai & Yue (1995) studied the mechanism of laminar vortices interacting with a contaminated surface at low Froude numbers. We concluded that the interactions are intermediate between, but qualitatively distinct from, those near a clean surface or a no-slip boundary. We also considered the effect of surfactant solubility and found that the surfactant effect are moderated by the sorption kinetics near the surface. Tsai (1996) extended this work to the case of a turbulent shear flow and found that the blocking effect by the surface is significantly reduced by surface contamination. He also found that attenuation of the surface fluid renewal by surfactants is responsible for a reduction of scalar exchange rate at the interface. Smith *et al.* (2001) studied the effects of a rising vortex pair on the thermal boundary layer at an air–water interface. Both simulations and measurements were performed and the results were found to be in good agreement. They related the variations of surface temperature to the underlying hydrodynamics and found that the surface straining rate is a controlling parameter.

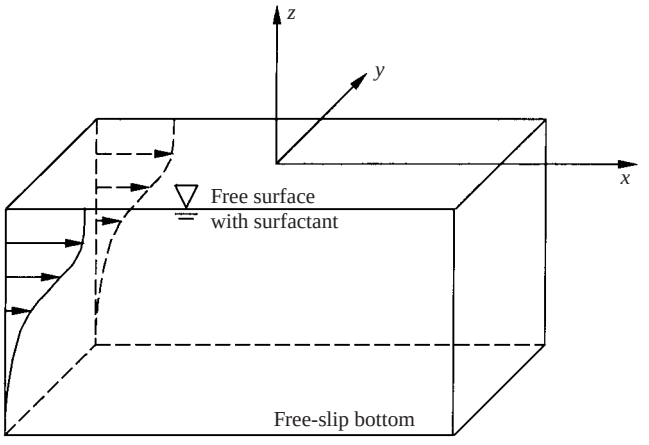

FIGURE 1. Schematic of a turbulent shear flow underneath a free surface.

For the turbulent shear layer underneath a clean stress-free surface, Shen *et al.* (1999) and Shen, Triantafyllou & Yue (2000) (hereinafter referred to as P1 and P2, respectively) performed a systematic DNS/analytic investigation. We found that near the free surface the turbulent flow exhibits a distinct multi-layer structure: as the surface is approached, the mean shear first increases over an outer layer and then decreases rapidly over an inner layer. Thus despite the fact that the free surface is shear free, the mean shear of the flow has a local peak just underneath the surface. To explain this phenomenon, P2 developed an analytic theory based on an assumption of self-similarity of the mean flow. The similarity solution was found to agree well with results of our direct numerical simulations. It also provides a quantitative definition for the surface boundary layers and scaling relationships for the surface-layer thickness, which were confirmed by simulations. This paper is an extension of P1 and P2 to the case where stress-free boundary conditions no longer obtain at the surface owing to the presence of surfactants.

The present study is both numerical and theoretical. We perform direct numerical simulations (DNS) for a turbulent shear flow under a surfactant-contaminated free surface. The ensemble DNS data are used to obtain the effects of surface elasticity on the free-surface boundary layer, the turbulence kinetic energy balance, and the near-surface vortical structures and their effect on surface deformation. Similar to P2, we then develop an analytic solution for the mean flow based on a similarity argument. The theoretical solution compares well with the simulation results. Based on this theoretical solution, we are able to deduce scaling laws for the boundary-layer thickness, which again agree well with the DNS data.

2. Problem definition and mathematical formulation

2.1. *Canonical problems and governing equations*

To investigate the effect of surfactant on turbulent flows, we consider as a canonical problem the interaction of a turbulent free shear flow with a surfactant-contaminated free surface (figure 1). The flow has a two-dimensional mean shear with an inflection in the velocity profile in the bulk flow. The shear rate vanishes at the free surface and in the deep region. Turbulence is first generated in the bulk flow because of inflection instability, and then interacts with the free surface. In this flow, there is

no mean pressure gradient (in other words, there is no horizontal body force). We assume that there is no external stress applied above the free surface, i.e. the wind stress is negligible. We also assume that the bottom is deep and its effect is small (in numerical simulations the bottom boundary is treated as a free-slip surface). As a result, as time evolves the shear flow is flattened out by diffusion, while the total momentum of the flow is constant in time.

As shown in figure 1, the frame of reference has axes x, y and z pointing in the mean flow streamwise, mean flow spanwise, and vertically upward directions, respectively. The origin is located at the undisturbed free surface. In this study we consider low Froude numbers so that the magnitude of surface deformation is small. This enables us to apply linearized free-surface boundary conditions at $z=0$.

The velocity components u_i (also denoted as u, v, or w) are governed by the Navier–Stokes equations and the continuity equation, which in tensor notation are:

$$\frac{\partial u_i}{\partial t}+\frac{\partial (u_i u_j)}{\partial x_j}=-\frac{\partial p}{\partial x_i}+\frac{1}{Re}\frac{\partial^2 u_i}{\partial x_j \partial x_j}, \quad i=1,2,3, \tag{2.1}$$

$$\frac{\partial u_i}{\partial x_i}=0. \tag{2.2}$$

Here and hereinafter, all variables are normalized by a characteristic length scale L_0 and a characteristic velocity scale U_0. As will be shown in § 2.2, the mean shear flow velocity profile at $t=0$ is used to define L_0 and U_0. The dynamic pressure p is normalized by ρU_0^2, where ρ is the fluid density. The Reynolds number is defined as $Re \equiv U_0 L_0/\nu$, with ν the kinematic viscosity.

The complete derivation of the free-surface boundary conditions for a Newtonian interface in the presence of surfactants can be found in Scriven (1960), Edwards *et al.* (1991) and Zhang (2001). We employ the linearized version, which is consistent with the assumption of small free-surface deformation. The linearized kinematic free-surface boundary condition is

$$\frac{\partial h}{\partial t}=w-\frac{\partial}{\partial x}(uh)-\frac{\partial}{\partial y}(vh) \qquad \text{on } z=0, \tag{2.3}$$

where h is the free-surface elevation.

The balance of normal and tangential stresses at the free surface is expressed in the following dynamic boundary conditions:

$$p=\frac{h}{Fr^2}+\frac{2}{Re}\frac{\partial w}{\partial z}-\left(\frac{\partial^2 h}{\partial x^2}+\frac{\partial^2 h}{\partial y^2}\right)\frac{\sigma}{We} \qquad \text{on } z=0, \tag{2.4}$$

$$\frac{1}{Re}\left(\frac{\partial u}{\partial z}+\frac{\partial w}{\partial x}\right)=\frac{1}{We}\frac{\partial \sigma}{\partial x} \qquad \text{on } z=0, \tag{2.5}$$

and

$$\frac{1}{Re}\left(\frac{\partial v}{\partial z}+\frac{\partial w}{\partial y}\right)=\frac{1}{We}\frac{\partial \sigma}{\partial y} \qquad \text{on } z=0. \tag{2.6}$$

Here $Fr \equiv U_0/\sqrt{gL_0}$ is the Froude number with g the acceleration due to gravity. The parameter $We \equiv \rho U_0^2 L_0/\sigma_0$ is the Weber number, while σ_0 is the equilibrium value of the surface tension in the absence of flow motion. In general, the surface tension σ (normalized by σ_0) in (2.4)–(2.6) varies in space and time because of variation in the surfactant concentration caused by flow motions. Let γ be the surfactant concentration normalized by the equilibrium (when the fluid is at rest) value γ_0. The equation

of state for the surface elasticity, which specifies the dependence of σ on γ is

$$\sigma - 1 = Ma(1 - \gamma). \tag{2.7}$$

Here $Ma \equiv (\gamma_0/\sigma_0)(\mathrm{d}\sigma/\mathrm{d}\gamma)\,|_{\gamma=1}$ is the Marangoni number of the surfactant, which measures the dependence of surface tension on the surfactant concentration. For a clean surface, Ma equals zero. For simplicity, σ is assumed to be a linear function of γ. This assumption is valid for small variation of γ, which is the case in our simulations. In general, the presence of surfactants also introduces other surface stresses associated with dilational and shear viscosities of the surfactant (see Edwards *et al.* 1991). For typical values of these (and for the quantities such as the mean flow characteristics we are interested in), the effects are found to be of only secondary importance compared to those due to surface elasticity (see e.g. Zhang 2001). In this work, for simplicity, we focus only on the effect of surface elasticity on the underlying turbulent flow.

The transport equation for $\gamma(x, y, t)$ is

$$\frac{\partial \gamma}{\partial t} + \frac{\partial (u\gamma)}{\partial x} + \frac{\partial (v\gamma)}{\partial y} - \frac{1}{Pe^s}\left(\frac{\partial^2 \gamma}{\partial x^2} + \frac{\partial^2 \gamma}{\partial y^2}\right) = 0 \qquad \text{on } z = 0, \tag{2.8}$$

where $Pe^s \equiv U_0 L_0/D^s$ is the surface Péclet number with D^s the surface diffusivity of the surfactant.

We use periodic conditions in the horizontal directions. At the bottom $z = -H$, we apply the free-slip condition

$$\frac{\partial u}{\partial z} = \frac{\partial v}{\partial z} = w = \frac{\partial p}{\partial z} = 0. \tag{2.9}$$

2.2. *Numerical method*

The numerical method of the DNS follows closely that in P1. The governing equations subject to the boundary conditions given in § 2.1 are solved using a finite-difference discretization. We use a sixth-order finite-difference scheme in the horizontal directions and a second-order scheme in the vertical direction. An explicit (second-order Runge–Kutta) time integration scheme is used. The pressure is solved via a Poisson equation, which is obtained by taking the divergence of (2.1) and involving (2.2) at the next time step. The only difference with P1 is the presence of additional Marangoni stress terms in the dynamic free-surface conditions and the transport equation (2.8) for the surfactant concentration. These are handled in a straightforward way in the finite-difference scheme. Note that we can take advantage of explicit time integration (which is cheaper computationally and simpler in treatment of the boundary conditions) because of the free-slip bottom boundary we impose. For cases with strong boundary shears such as open-channel flows, for example, fractional-step methods with implicit schemes for the viscous terms are usually required to prevent instability at the channel bottom (e.g. Kim & Moin 1985). We have applied both approaches to the present problem with identical results.

The simulation starts with an initial mean velocity profile

$$\frac{\langle u \rangle (z, t = 0)}{U_0} = \mathrm{sech}^2\left(0.88137 \frac{z}{L_0}\right). \tag{2.10}$$

Small-amplitude divergence-free velocity noise is imposed upon this initial field, serving as seeds for the turbulence. The profile (2.10) corresponds to the mean velocity measured in the wake of a NACA 0003 hydrofoil (Mattingly & Criminale 1972). The mean shear flow is unstable and energy is transfered from the mean flow to turbulence. We focus on the later stage of evolution when turbulence is fully

Grid	$q^2/2$	$\omega_i\omega_i/2$	$(\partial w/\partial z)^{rms}$	γ'^{rms}
$96^2 \times 128$	0.00260	0.276	0.00557	0.0469
$128^2 \times 192$	0.00279	0.317	0.00602	0.0518
$192^2 \times 256$	0.00282	0.307	0.00594	0.0528

TABLE 1. Comparison of surface values of turbulent kinetic energy, enstrophy, surface divergence fluctuation, and surfactant concentration fluctuation obtained using three different computational grids. $Ma = 0.1$ and $Re = 700$.

developed. As will be shown, at long times, the mean velocity acquires a self-similar profile.

In (2.10), $\langle u \rangle$ denotes the mean value of u. Throughout this paper, a mean value is consistently defined using plane-averaging because of the homogeneity of the flow in the horizontal directions. For later reference, for a physical variable $f(x, y, z, t)$, $\langle f \rangle(z, t)$ is the mean value; $f'(x, y, z, t) = f(x, y, z, t) - \langle f \rangle(z, t)$ denotes its fluctuation; and $f'^{rms}(z, t) = \sqrt{\langle f'(x, y, z, t)^2 \rangle}$ the root-mean-square fluctuation. To ensure statistical convergence, for each physical case we perform twenty-five independent simulations using different initial random seeds. The results presented in this paper are ensemble-averaged over the twenty-five DNS realizations.

Based on the scales U_0 and L_0 of the initial mean velocity profile (2.10), we consider three Reynolds numbers $Re = 700$, 1000 and 1400. The range of Re is limited in the DNS by the requirement of resolving all the length scales in the turbulent flow. We consider Froude numbers in the range $Fr = 0 \sim 0.7$. The Weber number is set to be 10. This range of parameters corresponds to water flows with velocity scale $O(10^{-1})\,\mathrm{m\,s^{-1}}$ and length scale $O(10^{-2})\,\mathrm{m}$.

To investigate the effects of surfactant elasticity, we repeat our simulations for a set of Marangoni numbers in the range $Ma = 0 \sim 0.2$ (the surface Péclet number Pe^s is set to be 1000). Marangoni numbers in this range are comparable with values (estimated by the ratio of measured surface elasticity to surface tension) in laboratory experiments involving synthetic and natural surfactants (e.g. Lopez & Hirsa 2000; McKenna 2000; Hirsa, Lopez & Miraghaie 2001; and Barger 1991; Frew & Nelson 1992; Frew 1997). The dependence of the results over the range of Ma is discussed in § 3.4. There is generally a (small) value of Ma (typically much less than 0.1) above which the results differ appreciably from those for a clean free surface (see e.g. figure 15). For definiteness, for most of the subsequent results, we choose $Ma = 0.1$ as the typical case to illustrate the effects of surfactant as compared to the clean $Ma = 0$ case.

The size of the computation domain is $L_x \times L_y = 10.472^2$ (horizontally) by $L_z = 6$ (vertically). We use a 128^2 (horizontal) $\times$ 192 (vertical) grid. The choice of these computation parameters and the numerical scheme have been validated in detail. Table 1 shows a typical example of the convergence test. The values of turbulent kinetic energy and enstrophy at the free surface, surface divergence fluctuation, and surfactant concentration fluctuation are compared among three different levels of computation resolution. The difference is found to be negligible. Additional convergence test results similar to P1 and P2 have also been obtained and will not be repeated in this paper.

3. Numerical results

In this section we present the DNS results. By comparing cases of $Ma = 0$ and $Ma = 0.1$, we show the effects of surfactants on surface-layer structure (§ 3.1), surface

divergence and free-surface signature (§ 3.2), and turbulent kinetic energy budget (§ 3.3). In § 3.4, we present a summary and discussions on the Marangoni-number dependence.

3.1. *Effects of surfactant on surface-layer structure*

We first present an overview of the flow field obtained from numerical simulation. For illustration purposes, we focus, unless otherwise indicated, on cases with $Re = 700$. The results of other Reynolds numbers will be presented and discussed in § 4. Figure 2 shows the time evolution of the profiles of mean velocity and turbulent kinetic energy. As time increases, the mean shear flow is flattened out by turbulence diffusivity and molecular viscosity. The instability mechanism of the shear flow transfers energy from the mean flow into turbulence. At a later stage of flow evolution, the turbulence is fully developed and turbulence production is roughly balanced by dissipation. In this study, we focus on this later stage.

Figure 2(*a*) represents the clean-surface case and figure 2(*b*) the contaminated-surface case. The slope of the mean velocity near the surface is much steeper in the contaminated-surface case than that in the clean-surface case. As was shown in P2, the mean shear variation offers a concise description of the free-surface boundary-layer structure.

Comparison between figures 2(*a*) and 2(*b*) reveals that the presence of surfactant reduces turbulent kinetic energy near the free surface. This reduction is caused by the surface elasticity of the surfactant which absorbs part of the turbulent kinetic energy of the fluid. Convection of turbulent fluid motions results in a non-uniform distribution of surfactant concentration, which affects the distribution of surface tension and creates gradients in surface-tension force. A typical example is shown in figure 3, which plots an instantaneous distribution of surfactant concentration $\gamma(x, y)$ and the surface-tension gradient $(\partial\sigma/\partial x, \partial\sigma/\partial y)$. High value of γ results in low value of σ so that the surface-tension force points from high γ regions to low γ regions. These surface-tension gradients serve as surface elasticity and they constrain horizontal motions u' and v' (plotted in figure 4).

The decrease of turbulence intensity near a surfactant-contaminated surface has been reported in several papers. For grid-stirred turbulence, McKenna (2000) found that the turbulence fluctuation velocity measured at a contaminated surface is about half of that at a clean surface. For evaporative convection at a surfactant surface, Flack *et al.* (2001)'s experimental measurements show that the turbulence kinetic energy obtains its maximum value at the clean surface, while for the surfactant case it is much damped and the maximum value is located away from the surface. Tsai (1996) obtained numerical velocity intensity profiles similar to those in figure 2, despite the fact that the Marangoni number he used ($Ma = 0.5$) is much higher than ours ($Ma = 0.1$). In § 3.4, we investigate the Marangoni number effects and show that, for high values of Ma, the variation of velocity intensity with Ma is small.

As discussed in P1, there exists a two-layer structure in the turbulence field near the free surface: the kinetic constraint of the surface on vertical motion creates a surface outer layer, within which velocity components are anisotropic; on the other hand, the dynamic free-surface boundary conditions create an inner layer where components of stress, vorticity, and vertical derivative of velocity are anisotropic. Figure 4 shows that the inner and outer layers are manifested in the DNS results for both the clean- and contaminated-surface cases. The turbulence statistics inside the surface layers are, however, substantially different between these two cases.

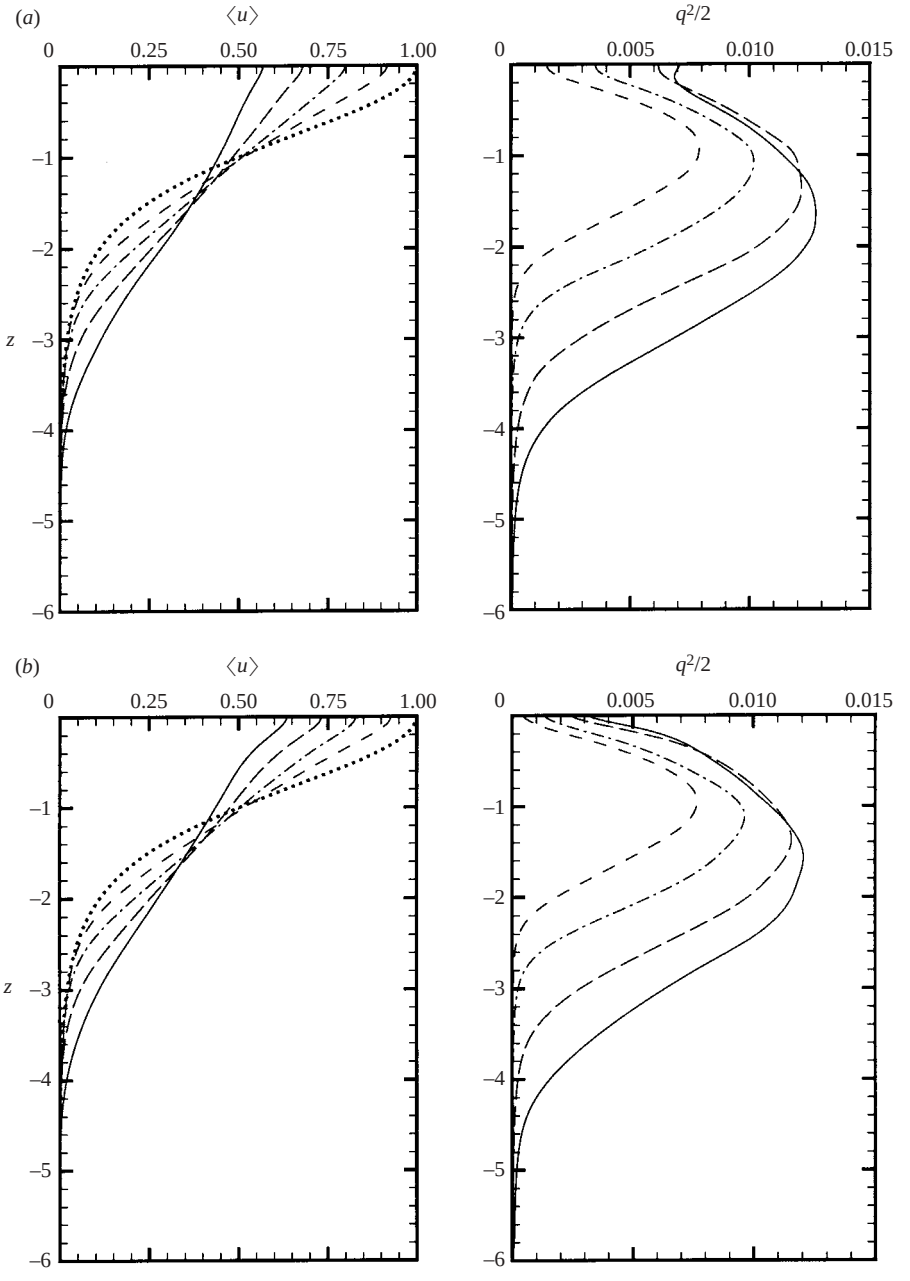

FIGURE 2. Time evolution of the profiles of the mean streamwise velocity $\langle u \rangle$ and the turbulent kinetic energy $q^2/2 \equiv \langle (u_i - \langle u_i \rangle)^2 \rangle / 2$, $i = 1, 2, 3$, for (*a*) the clean-surface case ($Ma = 0$); and (*b*) the contaminated-surface case ($Ma = 0.1$). · · · · · · , $t = 0$; – – – –, $t = 20$; – · – · – , $t = 40$; — —, $t = 60$; ————, $t = 80$.

Over the outer layer, fluctuation of the vertical velocity w'^{rms} diminishes towards the free surface. Near the clean surface, the variations of horizontal velocity components u'^{rms} and v'^{rms} are relatively small, because of the lack of constraint on horizontal motions. The surfactant-contaminated surface, however, possesses surface elasticity

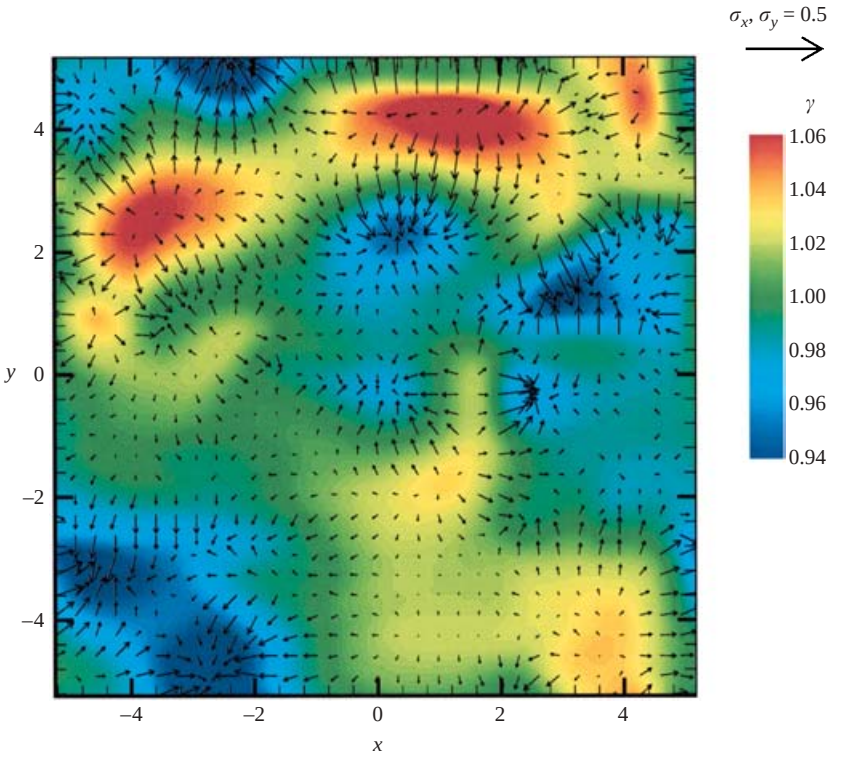

FIGURE 3. Instantaneous contours of surfactant concentration $\gamma(x, y)$ and distribution of surface-tension gradients $(\partial\sigma/\partial x, \partial\sigma/\partial y)$. Vectors of surface-tension gradients are plotted at every four grid points and their magnitude is proportional to the arrow length. $t = 70$.

which does not allow complete freedom in the horizontal motion. As a result, the magnitude of horizontal velocity u' and v' near a surfactant surface is smaller than that in the surfactant-free case (figure 4).

Inside the inner layer, as the free surface is approached, the tangential stress approaches the surface value specified by the dynamic boundary conditions (2.5) and (2.6). The surface value is zero for the clean-surface case, while for the surfactant case, it has large magnitude because of surface elasticity. In (2.5) and (2.6), since w is small near the surface, $\partial u/\partial z$ and $\partial v/\partial z$ dominate $\partial w/\partial x$ and $\partial w/\partial y$. As a result, the vorticity component has similar behaviour to the strain rate (or the stress). Figure 4 shows that inside the inner layer, horizontal vorticity components decrease towards a clean surface, but increase towards a contaminated surface. This sharp increase of horizontal vorticities is in agreement with the vorticity intensity profile shown in Tsai (1996). Figure 4, in addition, shows that the fluctuation of $\partial u/\partial z$ also behaves similarly near a surfactant surface.

3.2. *Effects of surfactant on instantaneous flow observables on the free surface*

The presence of surfactant directly affects the upwelling and downwelling fluid motions near a free surface. This can be seen by rewriting the surfactant transport equation (2.8) as

$$\frac{\partial\gamma}{\partial t} + u\frac{\partial\gamma}{\partial x} + v\frac{\partial\gamma}{\partial y} + \gamma\left(\frac{\partial u}{\partial x} + \frac{\partial v}{\partial y}\right) - \frac{1}{Pe^s}\left(\frac{\partial^2\gamma}{\partial x^2} + \frac{\partial^2\gamma}{\partial y^2}\right) = 0 \qquad \text{on } z = 0. \tag{3.1}$$

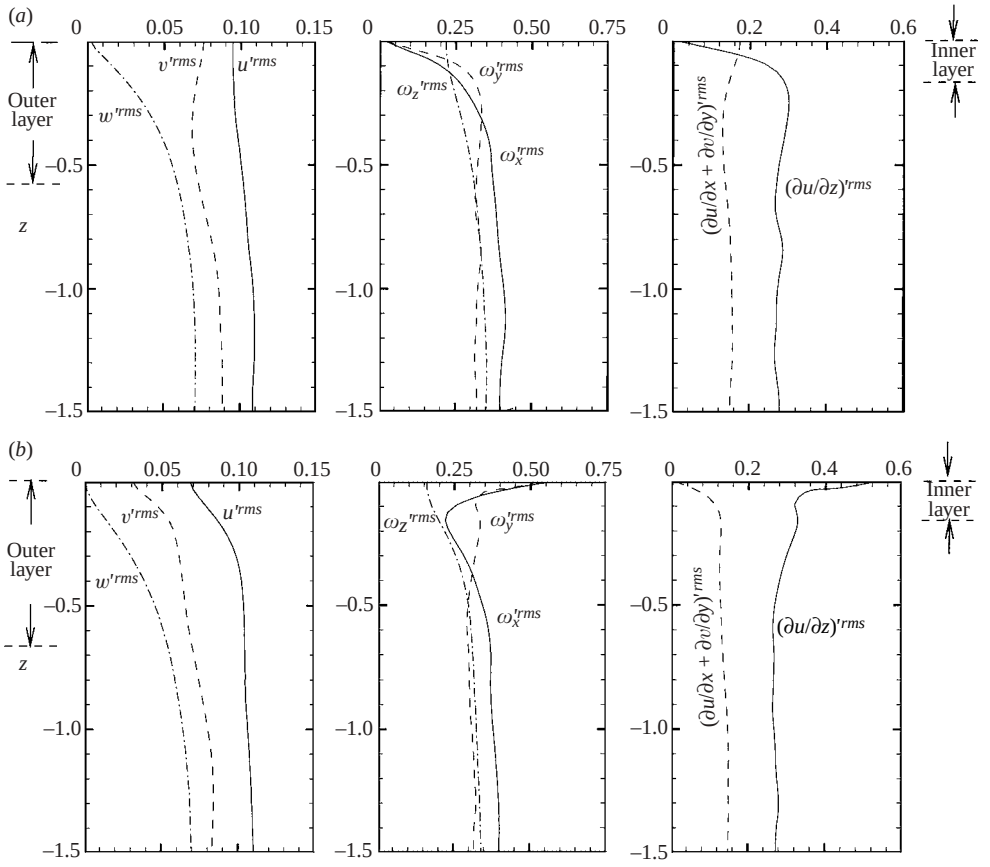

FIGURE 4. Profiles of fluctuation magnitude of velocity components $u_i'^{rms}$, vorticity components $\omega_i'^{rms}$, vertical gradients of velocity $(\partial u/\partial z)'^{rms}$, and surface divergence $(\partial u/\partial x + \partial v/\partial y)'^{rms}$, for (*a*) the clean-surface case $Ma = 0$ ($t = 60$); and (*b*) the contaminated-surface case $Ma = 0.1$ ($t = 70$).

The fourth term in the above, $\gamma(\partial u/\partial x + \partial v/\partial y) = -\gamma \partial w/\partial z$, measures the change in the surfactant concentration γ due to the upwelling ('splat' on the surface from below) and downwelling ('anti-splat' on the surface) of the flow. As γ changes, the surface tension σ also changes (equation (2.7)), which in turn creates a gradient of surface tension to counter the surface upwelling/downwelling motions. Figure 4 shows that the r.m.s. value of the surface divergence, $\partial u/\partial x + \partial v/\partial y$, which measures the strength of upwellings and downwellings, is substantially reduced when the free surface is contaminated by surfactants. For large *Ma*, Tsai (1996) reported on the time evolution of surface divergence at $z = 0$ where a similar conclusion can be obtained.

The effect of surfactant on surface divergence can also be seen clearly from the instantaneous flow field. Figure 5 plots the surface contour of $(\partial u/\partial x + \partial v/\partial y)|_{z=0}$ and velocity vectors $(u', v')|_{z=0}$. While splats (marked as 'A' and 'B') and anti-splats (marked as 'C') are manifested at the clean surface, they are lacking at the surfactant-contaminated surface.

The surface features shown in figure 5 are in excellent qualitative agreement with digital particle image velocimetry (DPIV) measurements by McKenna (2000) for oscillating grid-stirred turbulence under clean and surfactant surfaces. Figures 7–18(*a*)

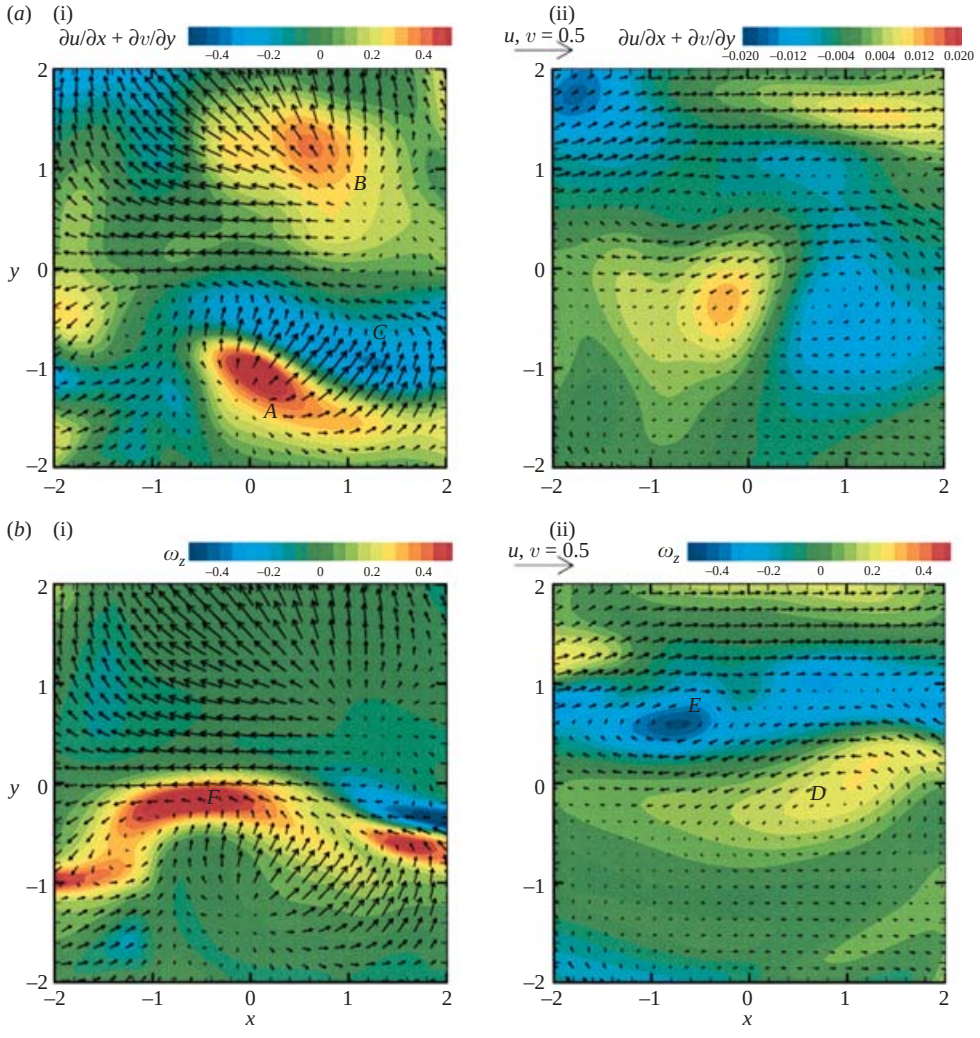

FIGURE 5. Vectors of (u', v') and (a) contours of surface divergence $\partial u/\partial x + \partial v/\partial y$, and (b) contours of surface-normal vorticity ω_z, at the free surface for (i) the clean-surface case ($Ma = 0$) and (ii) the contaminated-surface case ($Ma = 0.1$). Only partial regions of the free surface are plotted. $t = 70$. Note that the scales of $\partial u/\partial x + \partial v/\partial y$ are substantially different between the clean and contaminated cases.

and (b) there, which plot instantaneous velocity vectors and surface-normal vorticity, clearly show that the clean surface is dominated by surface bursting, while the surfactant case shows very weak flow divergence.

In figure 5, we also plot the contours of the vorticity normal to the free surface (selective surface-connecting vortices are marked as 'D', 'E' and 'F'). It is shown that the presence of surfactant reduces the magnitude of ω_z, but not by much. This fact can also be seen from the statistics of the r.m.s. value of ω_z plotted in figure 4. Similarly, for the velocity fluctuation (u', v'), only the portion associated with surface divergence is substantially reduced, while the portion corresponding to surface-normal vortical motion is less affected.

The disparate effects of surfactant on splats/anti-splats and surface-normal vorticity motions can be explained through (3.1), which shows that it is surface divergence not vorticity that enters as a source/sink term for the surfactant concentration. In summary, then, it is the decrease in surface divergence (rather than changes in velocity or vorticity fluctuations) that is the most prominent indicator and quantifier of the surfactant effects. Finally, we remark that near-surface turbulence diffusion processes are known to be strongly dependent on up-/downwelling at the surface (e.g. Jähne & Haussecker 1998). The present finding has a direct and significant implication to turbulence transport in the presence of surface contamination (Shen 2001).

3.3. *Effects of surfactant on the budget of turbulent kinetic energy*

We consider here the effects of surfactant on the budget of turbulent kinetic energy near the free surface. For turbulent flows with a mean sheared velocity $\langle u\rangle(z)$, the equations for the diagonal components of the Reynolds-stresses $\langle u'^2\rangle$, $\langle v'^2\rangle$ and $\langle w'^2\rangle$ are (see e.g. Hinze 1975, p. 323):

$$\frac{\partial\langle u'^2\rangle}{\partial t} = \underbrace{-2\langle u'w'\rangle\frac{\partial\langle u\rangle}{\partial z}}_{P_{uu}} + \underbrace{2\left\langle p'\frac{\partial u'}{\partial x}\right\rangle}_{\Phi_{uu}} - \underbrace{\frac{2}{Re}\left\langle\frac{\partial u'}{\partial x_k}\frac{\partial u'}{\partial x_k}\right\rangle}_{\varepsilon_{uu}} + \underbrace{\frac{1}{Re}\frac{\partial^2\langle u'^2\rangle}{\partial z^2}}_{D_{uu}} - \underbrace{\frac{\partial}{\partial z}\langle u'^2w'\rangle}_{T^v_{uu}}, \quad (3.2)$$

$$\frac{\partial\langle v'^2\rangle}{\partial t} = \underbrace{2\left\langle p'\frac{\partial v'}{\partial y}\right\rangle}_{\Phi_{vv}} - \underbrace{\frac{2}{Re}\left\langle\frac{\partial v'}{\partial x_k}\frac{\partial v'}{\partial x_k}\right\rangle}_{\varepsilon_{vv}} + \underbrace{\frac{1}{Re}\frac{\partial^2\langle v'^2\rangle}{\partial z^2}}_{D_{vv}} - \underbrace{\frac{\partial}{\partial z}\langle v'^2w'\rangle}_{T^v_{vv}}, \quad (3.3)$$

$$\frac{\partial\langle w'^2\rangle}{\partial t} = \underbrace{2\left\langle p'\frac{\partial w'}{\partial z}\right\rangle}_{\Phi_{ww}} - \underbrace{\frac{2}{Re}\left\langle\frac{\partial w'}{\partial x_k}\frac{\partial w'}{\partial x_k}\right\rangle}_{\varepsilon_{ww}} + \underbrace{\frac{1}{Re}\frac{\partial^2\langle w'^2\rangle}{\partial z^2}}_{D_{ww}} - \underbrace{\frac{\partial}{\partial z}\langle w'^3\rangle}_{T^v_{ww}} - \underbrace{2\frac{\partial}{\partial z}\langle p'w'\rangle}_{T^p_{ww}}. \quad (3.4)$$

Adding (3.2)–(3.4), we obtain the equation governing the evolution of the turbulent kinetic energy $\langle u_i'u_i'/2\rangle$:

$$\frac{\partial\langle u_i'u_i'/2\rangle}{\partial t} = \underbrace{-\langle u'w'\rangle\frac{\partial\langle u\rangle}{\partial z}}_{P_k} - \underbrace{\frac{1}{Re}\left\langle\frac{\partial u_i'}{\partial x_k}\frac{\partial u_i'}{\partial x_k}\right\rangle}_{\varepsilon_k} + \underbrace{\frac{1}{Re}\frac{\partial^2\langle u_i'u_i'/2\rangle}{\partial z^2}}_{D_k} - \underbrace{\frac{\partial}{\partial z}\langle(u_i'u_i'/2)w'\rangle}_{T^v_k} - \underbrace{\frac{\partial}{\partial z}\langle p'w'\rangle}_{T^p_k}. \quad (3.5)$$

In (3.5), P is the production rate; Φ the pressure–strain correlation; ε the dissipation rate; D the viscous diffusion; T^v the transport due to velocity fluctuations; and T^p is the transport due to pressure fluctuations. Note that the shear flow considered here varies rather slowly in time. As a result, the left-hand sides of (3.2)–(3.5) are small and the terms on the right-hand sides of each equation are in approximate balance.

Figure 6 plots the terms in the budget equations for both the clean- and contaminated-surface cases. We consider the effects of surfactants on each of these terms. In the shear flow, energy is extracted from the mean flow into turbulent motions through the production term P. Because the flow is statistically homogeneous in the horizontal directions and because the mean velocity is a function of z only, the streamwise velocity u' is the only component that receives energy directly from the

mean flow. The equations for $\langle v'^2 \rangle$ and $\langle w'^2 \rangle$ ((3.3 and (3.4)) do not have a production term. In general, P decreases as a clean surface is approached because of reduction of the vertical velocity fluctuation w' throughout the outer layer and the reduction of the mean shear rate $\partial \langle u \rangle / \partial z$ within the inner layer. Figure 6 shows that in the presence of surfactant, the production rate also decreases towards the surface, but at a rate faster than that of the clean-surface case. This can be attributed to the fact that the velocity fluctuations u' and w' are reduced by the elasticity of the surfactant surface. Further away from the surface, over the region of the outer layer, however, the production rate is larger in the contaminated-surface case. This is because the mean shear rate $\partial \langle u \rangle / \partial z$ is substantially enhanced beneath the contaminated surface (plotted in figures 16*a* and 19). The variation of the mean shear is investigated in detail in later sections of this paper (§§4.1–4.4).

After energy is transferred from the mean flow to the streamwise turbulent motions u', it is further redistributed among the three velocity components through the pressure–strain correlation term, Φ. In the bulk flow, as expected, Φ_{uu} is negative, while Φ_{vv} and Φ_{ww} are both positive (figure 6). As the free surface is approached, however, Φ_{ww} becomes negative and Φ_{uu} becomes positive. This variation is caused by the constraint of the surface on fluid vertical motions. In the presence of surfactants, because velocity fluctuations (of all the three velocity components) are reduced by surface elasticity, the magnitude of inter-component energy transfer is reduced at the near-surface region.

The term ε, which is always negative, measures the rate of energy dissipation due to viscosity. Figure 6(*d*) shows the significant difference caused by the presence of surfactants: the magnitude of ε decreases towards a clean surface, but increases when a surfactant-contaminated surface is approached. This can be explained by looking at the horizontal velocity components (figures 6*a* and 6*b*). As the dynamics boundary conditions ((2.5) and (2.6)) state, the values of $\partial u'/\partial z$ and $\partial v'/\partial z$ vanish at a clean surface. At a contaminated surface, however, the gradients in surface tension (shown in figure 3) need to be balanced by surface-tangential stresses, which results in non-zero values of $\partial u'/\partial z$ and $\partial v'/\partial z$. Consequently, the energy dissipation rate is enhanced substantially when the surface is contaminated.

The term D_k represents the viscous diffusion of turbulent kinetic energy, $\langle u_i' u_i'/2 \rangle$, in the vertical direction. It is determined by the profile of $\langle u_i' u_i'/2 \rangle(z)$ in which contributions from the horizontal velocity components dominate near the free surface. As a clean surface is approached, turbulent fluctuations increase slightly owing to the reduction in dissipation. The term D_k moves energy from the near-surface region to the region below. In the surfactant case, on the other hand, turbulent kinetic energy is smaller near the surface. Therefore, as figure 6 shows, the viscous diffusion D_k inputs a significant amount of energy at the surface.

Finally, the vertical transport due to turbulent velocity fluctuations is represented by the term T^v. In the equation for the vertical velocity component, the pressure fluctuations also contribute to the transport process, which is measured by the term T^p. Figure 6 shows that these terms are substantially different between the clean and contaminated cases. This is expected because of the different constraining mechanisms on the turbulent fluctuations by the surfaces. We also note that at a surfactant surface, unlike in the clean-surface case, the dissipation term ε and the viscous diffusion D dominate. This phenomenon resembles somewhat the flow near a solid wall where ε and D balance each other (Mansour, Kim & Moin 1988). The balance between ε and D is, however, not exact at a surfactant-contaminated free surface, and the difference is accounted for by the pressure transport term T^p.

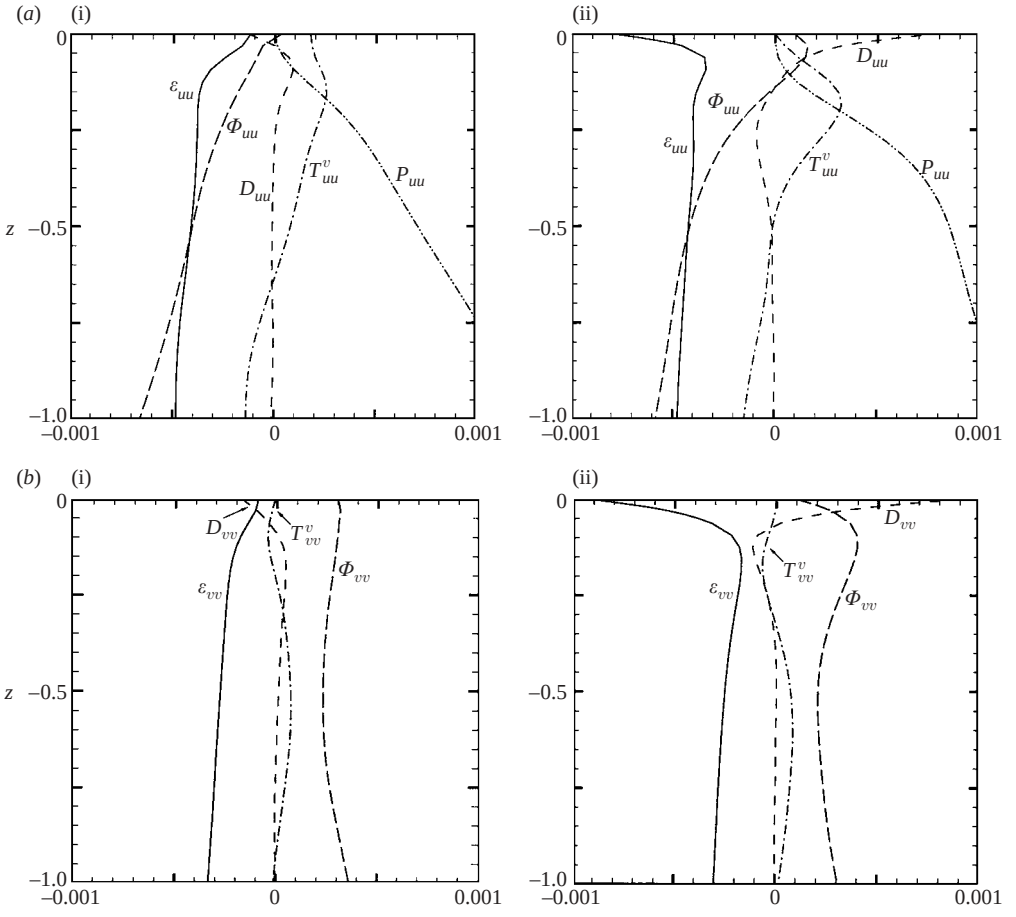

FIGURE 6(a, b). For caption see facing page.

The underlying mechanism for surfactant effects on the turbulent kinetic energy can also be explained in terms of coherent vortical structures. Figure 7(a) shows a snapshot of the vortical structures near a surface laden with surfactant. The vortical structures near the free surface are relatively simple and tracing vortex lines is easy and effective (we have also used other methods, for example, vortex identification based on eigenvalue of the velocity gradient tensor, obtaining essentially the same results).

Figure 7(a) shows three types of vortex structure: surface-connected vortices which terminate at the surface (almost perpendicularly at low Froude numbers); hairpin vortices with the 'head' located near the surface pointing in the y-direction and the two 'legs' extending to the bulk sheared flow; and Marangoni surface vorticity. The Marangoni surface vorticity is new in the presence of surfactants and is generated by the non-uniform distribution of surfactant concentration and surface tension. These vortices are comparable in magnitude to the other vortical structures in the flow and are generally in the form of closed rings just above and upstream of the hairpin vortices.

For statistics of the instantaneous vortex events such as those in figure 7, we employ a conditional-averaging technique to obtain ensemble-averaged data. The key idea of this method is to identify the turbulence structure of interest and then to

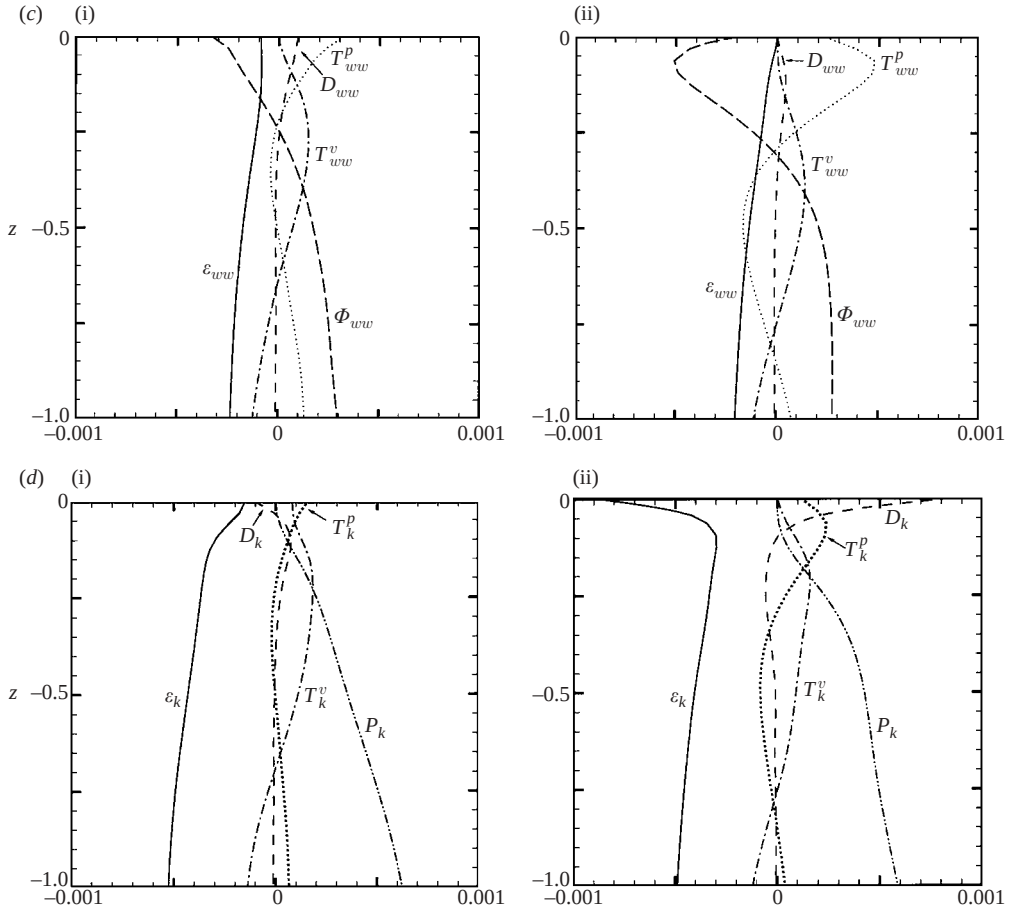

FIGURE 6. Terms in the turbulent fluctuation budget equations for (*a*) $\langle u'^2 \rangle$, (*b*) $\langle v'^2 \rangle$, (*c*) $\langle w'^2 \rangle$, and (*d*) $\langle u'_i u'_i / 2 \rangle$: P, production rate; Φ, pressure–strain correlation; ε, dissipation rate; D, viscous diffusion; T^v transport due to velocity fluctuations; T^p transport due to pressure fluctuations. (i) Clean surface; (ii) contaminated surface.

employ statistics for the flow field around the structures (e.g. the VITA method for experiments, Blackwelder & Kaplan 1976; and the VISA method in simulations, Kim 1983; Hartel *et al.* 1994; Piomelli, Yu & Adrian 1996).

Our interest here is the contributions of the hairpin and the Marangoni surface vorticity to the evolution of the turbulent kinetic energy. To obtain this, we define the event of interest to be when the head portion of hairpin vortices approach the surface. Since such events are characterized by large magnitudes of ω_y, we define the variable-interval space-averaging quantity:

$$\underline{\omega}_y(x, y, z, t, W) \equiv \frac{1}{4W^2} \int_{x-W}^{x+W} \int_{y-W}^{y+W} \omega_y(\xi, \zeta, z, t)\, \mathrm{d}\xi\, \mathrm{d}\zeta, \tag{3.6}$$

where W is the half width of the averaging window (set to be the macroscale of ω_y in the present case). To identify strong ω_y events, we use a localized variance

$$\omega_y^{var}(x, y, z, t, W) \equiv \omega_y^2(x, y, z, t) - \underline{\omega}_y^2(x, y, z, t, W). \tag{3.7}$$

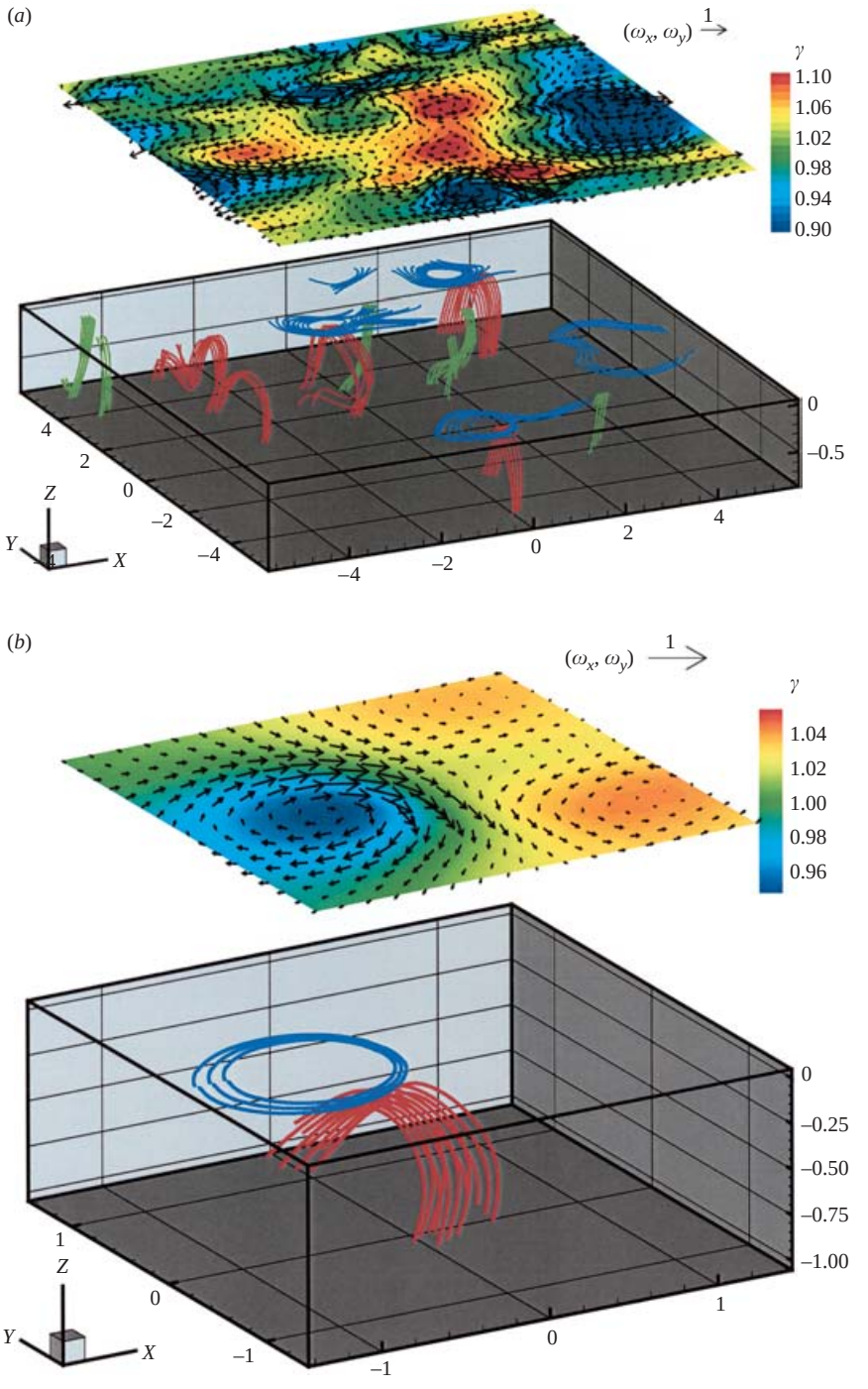

FIGURE 7. Distribution of surfactant concentration γ, surface vorticity (ω_x, ω_y) and coherent vortical structures (represented by vortex lines: green for surface-connected, red for hairpin, and blue for Marangoni surface vortices) in (*a*) an instantaneous flow field, and (*b*) the conditionally average flow field. Note that only select coherent vortices in the domain are plotted for illustration in (*a*).

Strong near-surface hairpin head events are detected if $\omega_y^{var} > c(\omega_y^{rms})^2$ at some (small) value of $z = Z$. In this case, the threshold level is set at $c = 15$ and the detection depth is set at $Z = -0.28$.

For each detected hairpin vortex event, the coordinates are transformed horizontally so that all the events are centred at $(0, 0, Z)$. Ensemble averaging is then performed. With due care in selecting the events, we show in figure 7(*b*) the results after averaging over 2000 events. Compared to figure 7(*a*), the conditionally averaged data is much smoother, while both the hairpin vortex and the accompanying Marangoni surface vorticity are captured faithfully.

Figures 8 and 9 show features of the conditionally averaged flow field (figure 7*b*) on the vertical section $(x, z; y = 0)$ and at the free surface $(x, y; z = 0)$, respectively. For both the clean and contaminated surface cases, the head portion of the hairpin vortices (positive ω_y) is shown clearly in the ω_y contours plotted in figure 8(*b*). Because of flow induction by the head and legs of the hairpin vortices, fluid particles upstream of the hairpin are swept towards the surface (figure 8*a*), causing a splat at the surface (figure 9*a*).

The events associated with figures 8 and 9 turn out to be the main mechanism of transfer of turbulence energy to surface deformations. Figure 9(*b*) shows that the surface is elevated just upstream of the hairpin vortex where upwelling occurs. Above the vortex, the surface is depressed by the fluid vortical motions. Comparison between the clean and contaminated cases, however, shows that the further effect of surfactants on the free-surface elevation is small. This is confirmed in the time evolution of h^{rms} in figure 10. As expected, h^{rms} scales with Fr^2 (the small values of h^{rms}/Fr^2 are due to the normalization of Fr by the mean flow velocity and not that of the turbulence fluctuations) and the presence of surfactants (slightly) reduces h^{rms}. The initial rise and subsequent later-time decrease of h^{rms} can be readily explained in terms of the evolution of the bulk flow turbulence kinetic energy. Finally we note that while the effect of the flow on the surface deformation is manifest, the effect of free-surface elevation on the underlying turbulence is small for the Froude-number range we consider, for both the clean (see P1) and contaminated surfaces.

Figure 9(*b*) also shows the vector plots of the surface vorticity. The surface vorticity caused by surfactant (the Marangoni surface vorticity) in this case is two orders of magnitude larger than that on the clean surface. The natures of these vortices are different. At a clean surface, surface vorticity is entirely associated with surface deformation (Batchelor 1967; Longuet-Higgins 1998) which, at the present low Froude numbers, is small. The Marangoni surface vorticity, however, is generated by variation in the surface tension. From (2.5)–(2.7), we obtain the Marangoni surface vorticity

$$\left.\begin{aligned} \omega_x &\approx -\frac{Re}{We}\frac{\partial \sigma}{\partial y} = \frac{ReMa}{We}\frac{\partial \gamma}{\partial y}, \\ \omega_y &\approx \frac{Re}{We}\frac{\partial \sigma}{\partial x} = -\frac{ReMa}{We}\frac{\partial \gamma}{\partial x}, \end{aligned}\right\} \tag{3.8}$$

which are tangent to the contour lines of the surfactant concentration (figure 9*c*). Upstream of the hairpin vortex, surfactant concentration is decreased by the upwelling resulting in a circular region of lower γ with ring-like contours (figures 7 and 9*c*). The resultant Marangoni surface vorticity is thus also ringlike, just upstream of a rising hairpin, and has an opposite sign to that of the hairpin in the region near the hairpin head (see figure 8*b*).

We remark that the Marangoni surface vorticity in the present three-dimensional flow is weaker than the same vorticity obtained in two-dimensional studies (e.g. Bernal

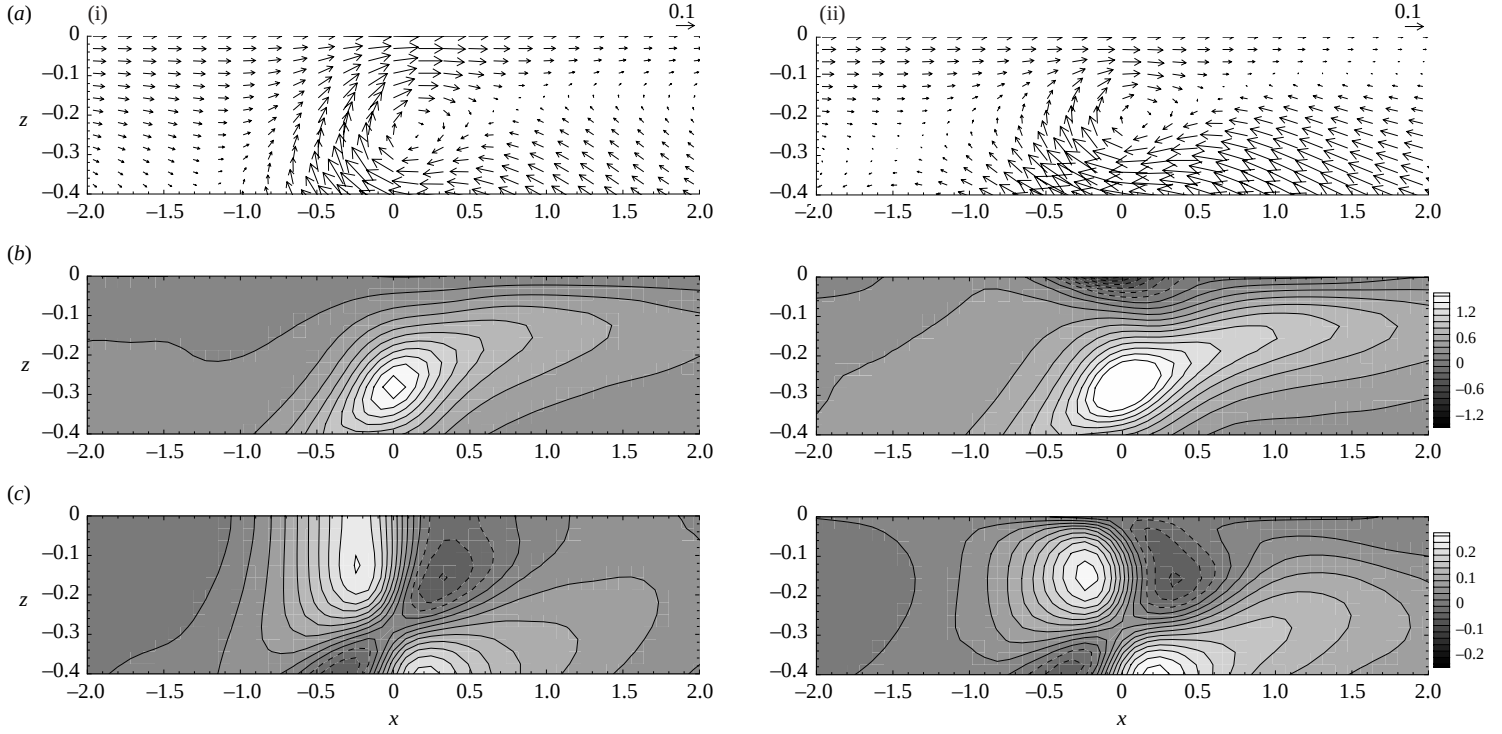

FIGURE 8. (*a*) Velocity vectors (u', w'), (*b*) contours of transverse vorticity ω_y, and (*c*) contours of horizontal divergence $(\partial u/\partial x + \partial v/\partial y)$ on the vertical section $(x, z; y = 0)$ in the conditionally averaged flow field. (i) Clean surface; (ii) contaminated surface. Dashed contour lines represent negative values. A constant value is subtracted from all the velocity vectors (Galilean transform) to illustrate better the occurrence of the splat.

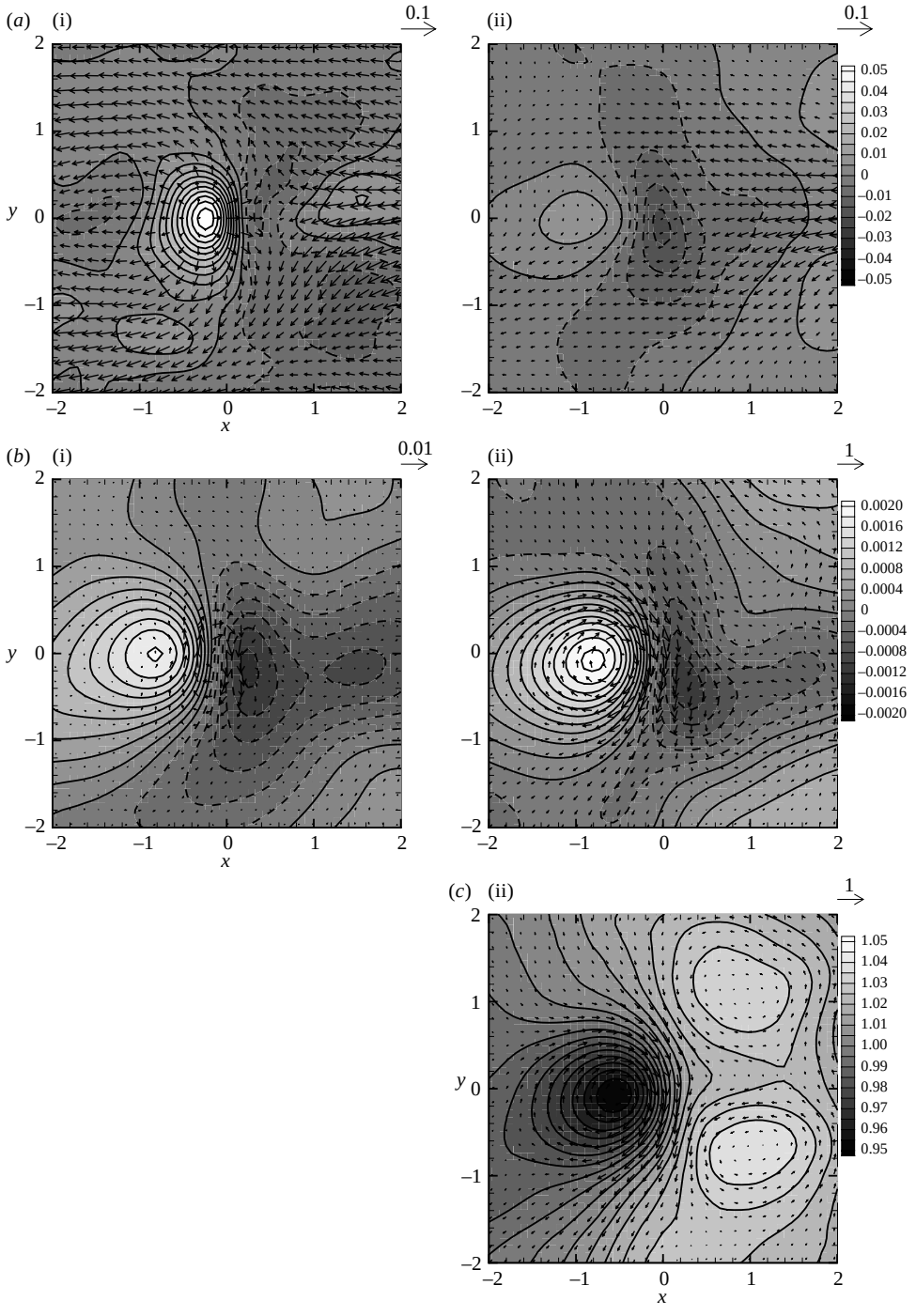

FIGURE 9. (*a*) Velocity vectors (u', v') and contours of surface divergence $(\partial u/\partial x + \partial v/\partial y)$, (*b*) contours of free-surface elevation h and vectors of surface vorticity (ω_x, ω_y), and (*c*) contours of surfactant concentration γ and vectors of surface vorticity (ω_x, ω_y) at the surface of the conditionally averaged flow field. $Fr = 0.707$. (i) Clean surface; (ii) contaminated surface. Dashed contour lines represent negative values. A constant value is subtracted from all the velocity vectors (Galilean transform) to illustrate better the occurrence of the splat.

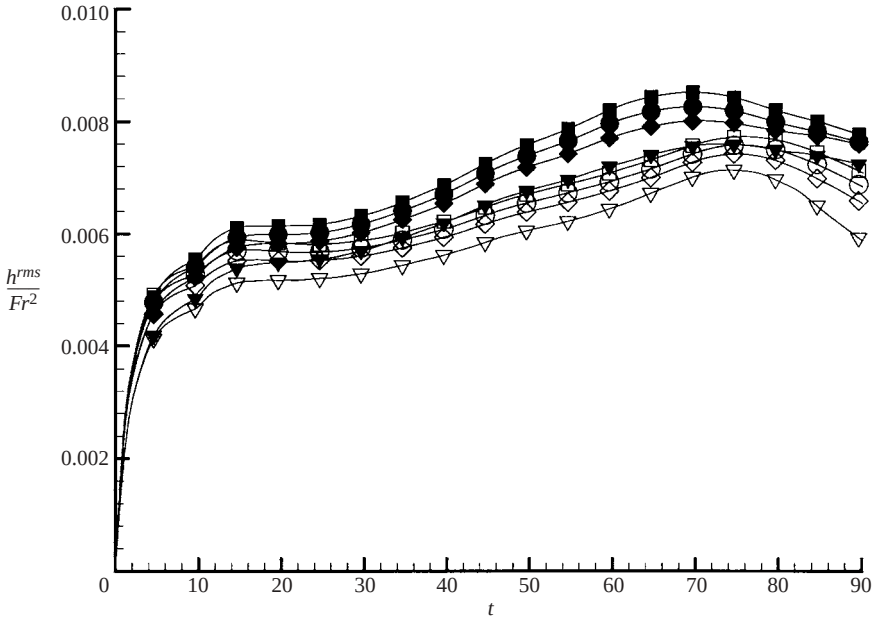

FIGURE 10. Time evolution of free-surface-elevation fluctuation h^{rms}/Fr^2. Box, $Fr = 0.1$; circle, $Fr = 0.3$; diamond, $Fr = 0.447$; triangle, $Fr = 0.707$. Filled and hollow symbols represent clean and contaminated surfaces, respectively.

et al. 1989; Hirsa & Willmarth 1994; Tsai & Yue 1995; Smith *et al.* 2001). One indicator is the surface concentration where figure 9(*c*) shows only a small reduction of γ, whereas in Tsai & Yue (1995), for example, a pair of rectilinear vortices approaching the surface is able to create a 'clean hole' in the upwelling region. Consequently, strong surfactant-flow interaction features such as rebounding of the primary vortex and wrapping of the secondary vortex around the primary one are not observed here. Instead we still observe vortex connection similar to that observed in the clean-surface case (shown in P1).

Despite the above, the presence of Marangoni surface vorticity has a substantial impact on the underlying flow, notably in decreasing the magnitude of the upwellings. The drastic reduction of surface divergence near a surfactant surface can be seen from horizontal velocity vectors (u', v') and contours of surface divergence $(\partial u/\partial x + \partial v/\partial y)$ plotted in figure 9(*a*), as well as the contours of $(\partial u/\partial x + \partial v/\partial y)$ on the vertical section (figure 8*c*).

The upwellings associated with hairpin vortices and their reduction by Marangoni surface vorticity directly affect the budgets of Reynolds stresses and turbulence kinetic energy. Figure 11 plots the distributions of the pressure–strain correlation terms, $p'\partial u'/\partial x$, $p'\partial v'/\partial y$ and $p'\partial w'/\partial z$, which measure the energy redistribution among different velocity components. Away from the surface, the inter-component energy redistributions are similar with or without surfactants. At a splat, energy goes from the vertical to the horizontal (Perot & Moin 1995; Walker, Leighton & Garza-Rios 1996) with, however, more of it going into the transverse versus streamwise component (Handler *et al.* 1993). Because of the present free shear-flow, such horizontal anisotropy is expected, while for open-channel flows, the anisotropy would be diminished for higher Reynolds numbers (Calmet & Magnaudet 2003). The mechanism for this

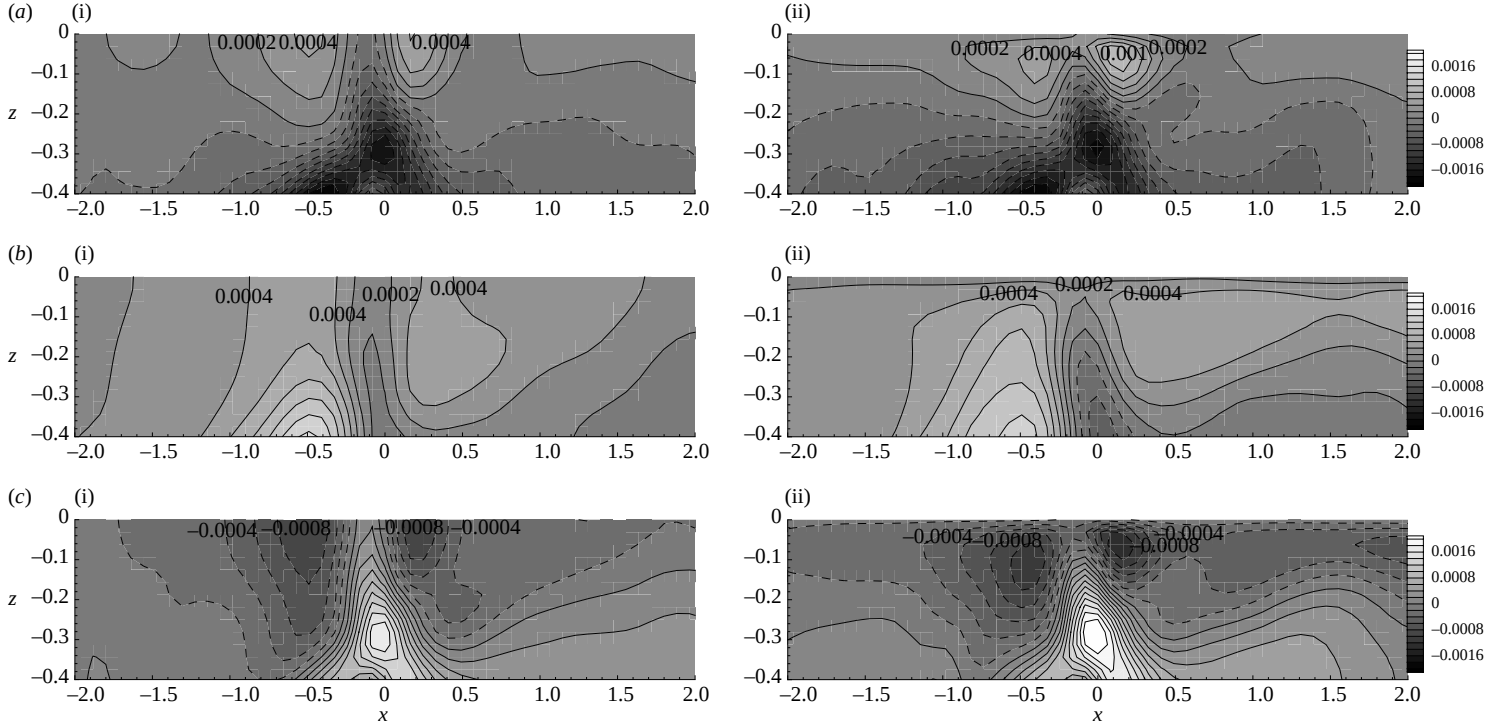

FIGURE 11. Contours of the pressure–strain correlation terms (*a*) $p'\partial u'/\partial x$, (*b*) $p'\partial v'/\partial y$, and (*c*) $p'\partial w'/\partial z$ in the conditionally averaged flow field. (i) Clean surface; (ii) contaminated surface. Dashed contour lines represent negative values.

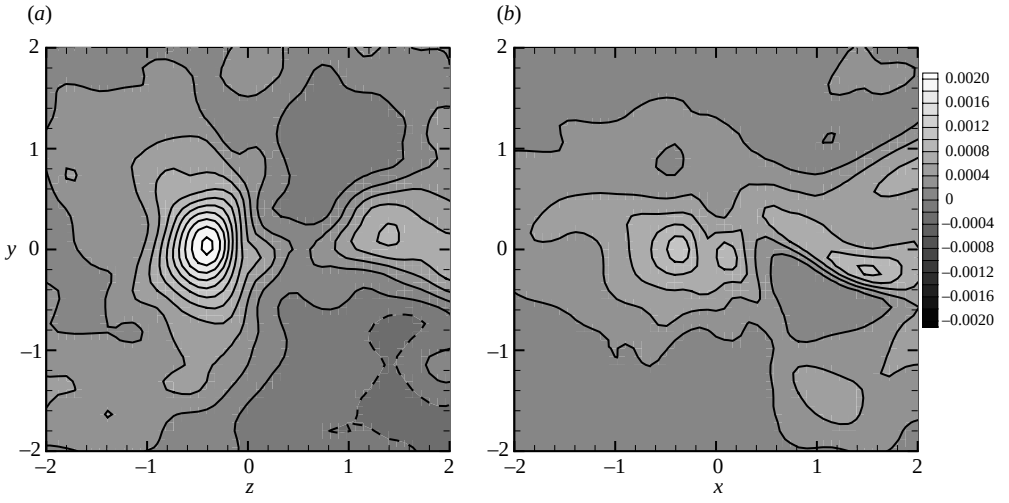

FIGURE 12. Contours of the transport terms $-\partial(u_i'^2 w'/2)/\partial z$ on the horizontal plane $(x, y; z \approx -0.03)$ in the conditionally averaged flow field. (*a*) Clean surface; (*b*) contaminated surface.

horizontal anisotropy is now understood in terms of the dynamics of coherent vortex structures and their interactions with the free surface (Nagaosa 1999). Such anisotropy can also be observed in more complex free-surface flows such as the flow in the corner between a free surface and a solid wall (see e.g. Broglia, Pascarelli & Piomelli 2003). In the presence of surfactants, the magnitudes of the pressure–strain correlation terms are greatly reduced because of the suppression of surface divergence. A very similar mechanism is also responsible for the drastic reduction in the turbulent transport near the surface as shown in figure 12 in the upward transport upstream of the upwelling.

In contrast to the above, the turbulence dissipation and viscous diffusion terms are enhanced in the presence of surfactant. Figure 13 shows the large dissipation above the hairpin vortex in the region with large gradients in surface tension, and large Marangoni surface vorticity or shear (figure 8). The latter has been observed in other free-surface surfactant flows, e.g. the vortex pair (Smith *et al.* 2001), submerged turbulent jet (Anthony *et al.* 1991), and flow with a stagnant film (Scott 1982; Harber & Gulliver 1992; Warncke, Gharib & Roesgen 1996). Since viscous diffusion is associated with the vertical variation of the fluctuation magnitude, this diffusion is enhanced near the surface by surfactant, which restricts the fluid motion on the surface (figure 14).

3.4. *Summary and discussion on Marangoni-number dependence*

In the previous subsections, we elucidate the important effects of surface contamination by comparing the results for $Ma = 0.1$ with those of a clean free surface ($Ma = 0$). These include: (*a*) decrease in velocity fluctuations; (*b*) increase in surface-tangential vorticities and decrease in surface-normal vorticity; (*c*) substantial decrease in surface divergence; and (*d*) increase in the dissipation and viscous diffusion of the turbulent kinetic energy and decrease in the energy production, pressure–strain redistribution, and turbulence transport.

In practice, the Marangoni number can vary over a large range. Our direct simulations show that the above effects are generally manifest when Ma increases beyond a small value. The magnitudes of these effects continue to grow with increasing Ma

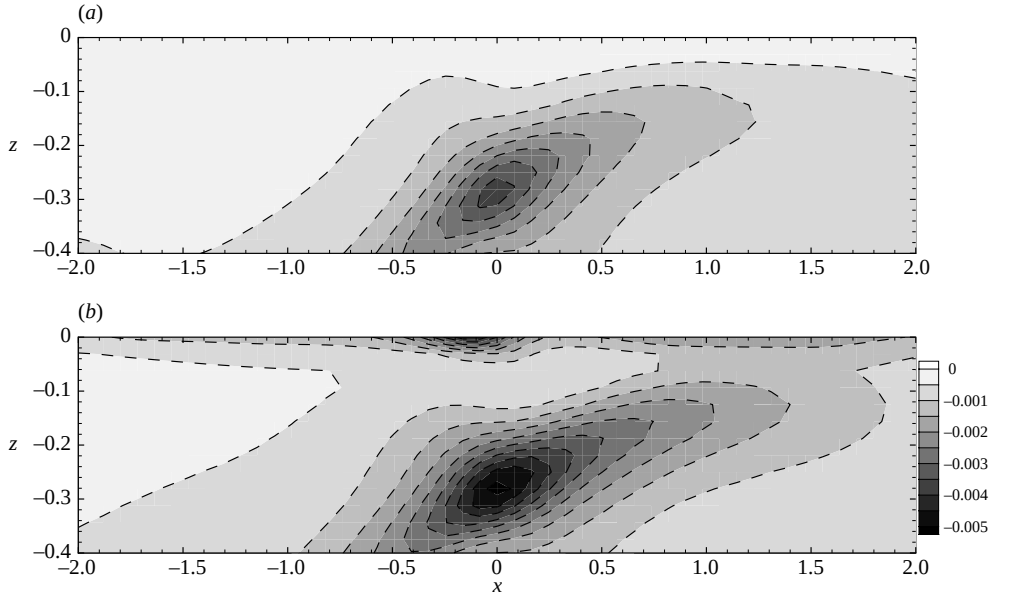

FIGURE 13. Contours of the dissipation term $(\partial u_i'/\partial x_k)^2/Re$ in the conditionally averaged flow field. (*a*) Clean surface; (*b*) contaminated surface.

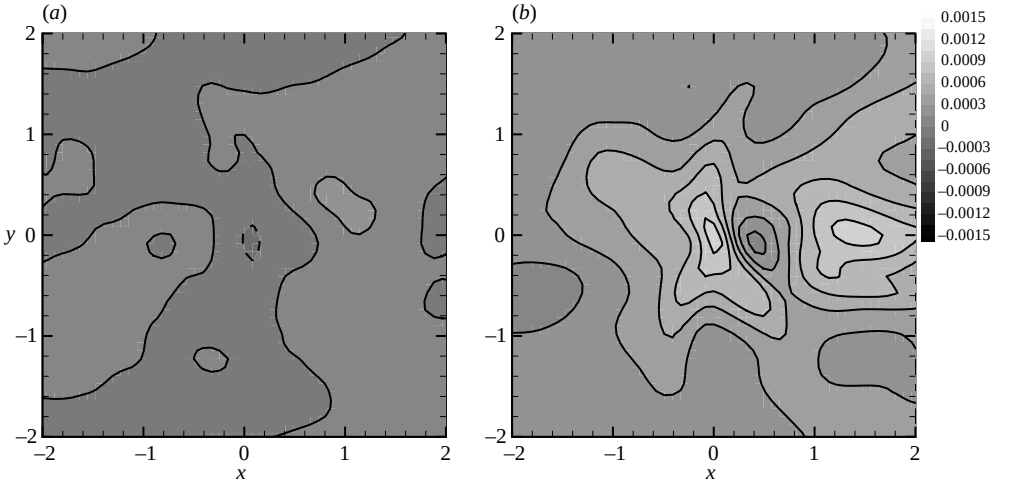

FIGURE 14. Contours of the viscous diffusion term $(\partial^2(u_i'^2/2)/\partial z^2)/Re$ on the horizontal plane $(x, y; z \approx -0.03)$ in the conditionally averaged flow field. (*a*) Clean surface; (*b*) contaminated surface.

and may (eventually) saturate even for moderate *Ma* (beyond which further increase in *Ma* has no appreciable effect). Figure 15 plots the ratios of contaminated ($Ma > 0$) to clean surface ($Ma = 0$) values of several typical surface quantities discussed in §§3.1–3.3 for a range of *Ma* (plotted on a logarithmic scale).

As the Marangoni number is increased, both u'^{rms} and $\omega_z'^{rms}$ are reduced gradually. Their values at high *Ma* are still comparable to the values in the clean surface case. The surface divergence, on the other hand, is much more sensitive to the Marangoni

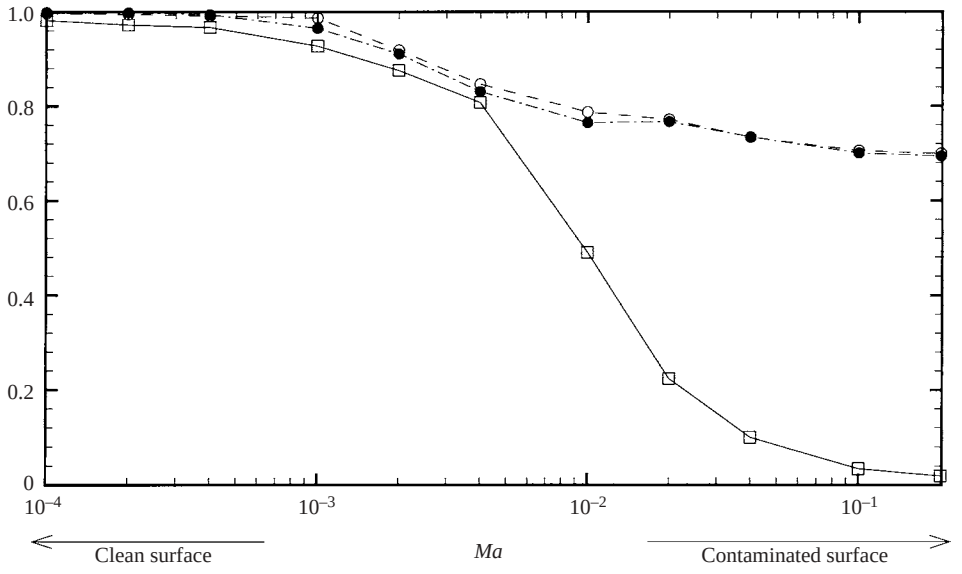

FIGURE 15. Ratios of the contaminated to the clean surface values of u'^{rms} (○), $\omega_z'^{rms}$ (●), and $(\partial u/\partial x + \partial v/\partial y)'^{rms}$ (□) at the surface, as functions of *Ma*.

number. It starts to drop sharply as *Ma* exceeds a small value around 0.005. This sensitivity to small Marangoni number value is in agreement with the results of Smith *et al.* (2001) who found that for their two-dimensional case, the surfactant effects are prominent even for $Ma \sim 10^{-3}$. For higher *Ma*, say $Ma \tilde{>} 0.05$, the r.m.s. value of the surface divergence is close to zero. Thus, as shown in § 3.2, the surface divergence is the most prominent feature of surfactant effects we have found. This effect results in a qualitative change in the fluid upwelling and downwelling motions.

4. Theoretical consideration

The DNS results in § 3 show the prominent effects of surfactants on turbulent flows. To understand the underlying mechanisms better and to obtain a precise and convenient description of the surface-layer structure, we obtain here a theoretical framework for the surfactant effects on the mean flow. We first derive a similarity solution to quantify the multi-layer structure of the surface boundary layer (§ 4.1). The predictions of the similarity solution are then verified against direct numerical simulations (§ 4.2). Based on this analytic solution, we obtain in § 4.3 the scaling laws for the thickness of the respective surface layers. These are also confirmed using DNS results.

4.1. *An analytic similarity solution for the mean flow*

In P2, we found that the structure of the turbulent boundary layer near a clean surface can be characterized by the profile of the mean shear rate. As the free surface is approached, the shear rate first increases over the outer layer and then decreases quickly over the inner layer. In the presence of surfactants, this qualitative description still obtains, but the variation of the mean shear is much sharper (figure 16*a*).

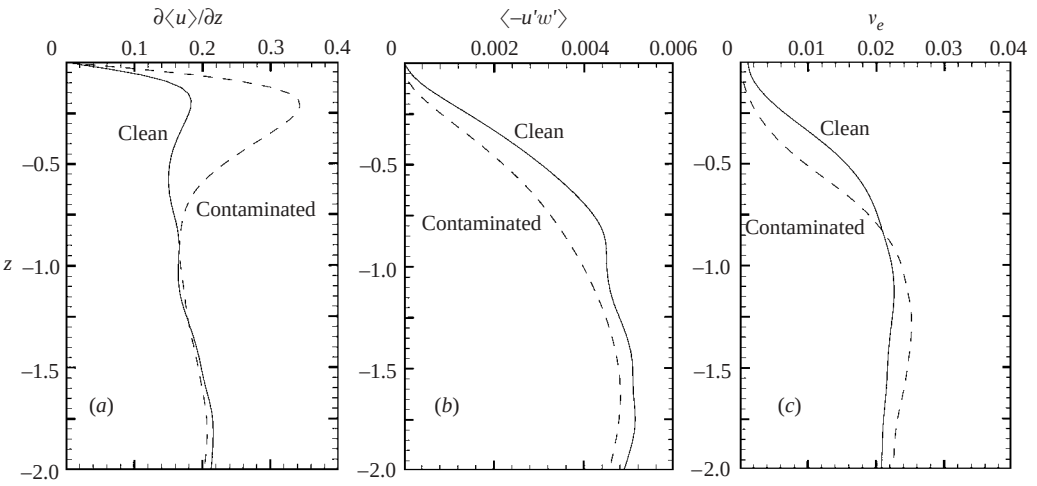

FIGURE 16. Profiles of (*a*) the mean shear rate $\partial\langle u\rangle/\partial z$; (*b*) the Reynolds stress $\langle -u'w'\rangle$; and (*c*) the eddy viscosity ν_e. ————, the clean-surface case $Ma = 0$ ($t = 60$); – – –, the contaminated-surface case $Ma = 0.1$ ($t = 70$).

We take plane averaging of the x-momentum equation and obtain the governing equation for the mean flow:

$$\frac{\partial\langle u\rangle}{\partial t} = -\frac{\partial\langle u'w'\rangle}{\partial z} + \frac{1}{Re}\frac{\partial^2\langle u\rangle}{\partial z^2} = \frac{\partial}{\partial z}\left(\left(\frac{1}{Re} + \nu_e\right)\frac{\partial\langle u\rangle}{\partial z}\right). \tag{4.1}$$

Here, the eddy viscosity ν_e (normalized by $U_0 L_0$) is defined based on the Reynolds stress $\langle -u'w'\rangle$ and the mean shear rate $\partial\langle u\rangle/\partial z$:

$$\nu_e \equiv \frac{\langle -u'w'\rangle}{\partial\langle u\rangle/\partial z}. \tag{4.2}$$

Figure 16 also plots the profiles of $\langle -u'w'\rangle$ and ν_e. Both the Reynolds stress and the eddy viscosity decrease as the free surface is approached, because of the constraint of the surface on the vertical motion w'. Figure 16(*c*) shows that at the clean surface, the value of ν_e is small but non-zero. P2 argued that the eddy viscosity has a value very close to the value of the molecular viscosity at a clean free-surface (this was also shown by the results of Nagaosa 1999). At the contaminated surface, on the other hand, figure 16(*c*) shows that the eddy viscosity has a value much smaller than the molecular viscosity. This has an appreciable effect on the structure of the boundary layer.

At the free surface, horizontal averaging of the dynamic boundary condition (2.5) yields

$$\frac{\partial\langle u\rangle}{\partial z} = 0 \qquad \text{on } z = 0. \tag{4.3}$$

Note that in the presence of surfactants, although locally $\partial u/\partial z$ at the surface may fluctuate because of surface elasticity (figure 4), the gradients in the surface tension (equation (2.5)) serve as internal forces when plane-averaging is performed and therefore on average the surface is shear free. Because of the vanishing of $\partial\langle u\rangle/\partial z$, at the free surface we obtain a special form of eddy viscosity by applying l'Hopital's

rule to (4.2):

$$\nu_e|_{z=0} = \frac{\partial\langle -u'w'\rangle/\partial z|_{z=0}}{\partial^2\langle u\rangle/\partial z^2|_{z=0}}. \tag{4.4}$$

Note that at a boundary where the mean shear is non-zero, such as a solid wall or a sheared air–water interface, (4.2) yields a zero eddy viscosity. At a shear-free surface, however, ν_e is not necessarily zero and its value must be calculated from (4.4).

As shown above, the governing equation and the free-surface boundary condition for $\langle u\rangle$ are effectively the same for the clean-surface case and the surfactant-contaminated case, and we can obtain a self-similar solution for $\langle u\rangle$ in a way identical to the clean-surface case. The complete derivation of the similarity solution for a clean surface was given in P2, and here we present the results only.

The mean velocity profile is described by a self-similar form

$$\frac{\langle u\rangle - U_\infty}{U_d} = f(\eta), \tag{4.5}$$

where $U_d = \langle u\rangle|_{z=0} - U_\infty$ is the velocity deficit, with $U_\infty \equiv \langle u\rangle|_{z\to-\infty}$. In our simulation, we set the free-slip bottom (cf. figure 1) to be sufficiently deep so that $U_\infty = U_{z=-H} \approx 0$ at all times considered in this paper. In (4.5), η is the similarity variable

$$\eta = z/b, \tag{4.6}$$

with b measuring the extent of the mean shear in the flow. Note that both U_d and b are functions of time.

The eddy viscosity is expressed as

$$\frac{\nu_e}{U_d b} = \psi(\eta), \tag{4.7}$$

where ψ is some function of the similarity variable, and it measures the variation of eddy viscosity as the free surface is approached. We denote by ψ_a the value of ψ well below the free surface, i.e. outside the outer layer; and by ψ_0 the value of ψ at the free surface.

Similar to P2, we derived that

$$U_d b = C_0, \tag{4.8}$$

$$b = \sqrt{2(\nu + U_d b\psi_a)t + Q}, \tag{4.9}$$

and

$$U_d = \frac{C_0}{\sqrt{2(\nu + U_d b\psi_a)t + Q}}, \tag{4.10}$$

where C_0 and Q are constants.

The shape of the mean velocity profile is

$$f(\eta) = \exp\left(-\int_0^\eta \frac{s(\nu + U_d b\psi_a)}{\nu + U_d b\psi(s)}\,\mathrm{d}s\right). \tag{4.11}$$

Equation (4.11) provides the dependence of the mean flow profile on the variation of eddy viscosity as a function of the distance from the free surface. It contains the essential physics of turbulent diffusion near the surface and forms a basis for our analysis.

	$Re = 700$			$Re = 1000$			$Re = 1400$		
t	U_d	b	C_0	U_d	b	C_0	U_d	b	C_0
70	0.683	1.741	1.189	0.627	1.831	1.149	0.608	1.876	1.141
75	0.659	1.802	1.187	0.604	1.892	1.142	0.587	1.940	1.140
80	0.635	1.864	1.184	0.582	1.959	1.140	0.568	1.997	1.134
85	0.612	1.927	1.179	0.562	2.031	1.142	0.550	2.057	1.132
90	0.590	1.999	1.179	0.544	2.102	1.144	0.533	2.127	1.134

TABLE 2. Variation with time of the mean velocity deficit U_d, the mean shear extent b, and the product $C_0 = U_d b$, for different Re. $Ma = 0.1$.

It is found that the eddy viscosity profile (figure 16) can be approximated by a Gaussian profile:

$$\psi = \frac{\nu_e}{U_d b} = \psi_a - (\psi_a - \psi_0)\exp(-\eta^2/a^2)$$
$$= \begin{cases} \psi_a - \left(\psi_a - \dfrac{1}{C_0 Re}\right)\exp(-\eta^2/a^2) & \text{clean surface,} \\ \psi_a - \psi_a \exp(-\eta^2/a^2) & \text{contaminated surface,} \end{cases} \tag{4.12}$$

where a is the thickness of the outer layer normalized by the shear flow extent b. Note that (4.12) is consistent with the eddy viscosity having the value of molecular viscosity ($\psi_0 = 1/(C_0 Re)$) at a clean surface, and being negligibly small ($\psi_0 \approx 0$) at a contaminated surface.

Finally, using (4.12), we obtain from (4.11):

$$f(\eta) = \exp(-\eta^2/2)\left[\frac{1/(C_0 R_e) + \psi_0}{1/(C_0 R_e) + \psi_a - (\psi_a - \psi_0)\exp(-\eta^2/a^2)}\right]^{a^2/2}$$
$$= \begin{cases} \exp(-\eta^2/2)\left[\dfrac{2/(C_0 R_e)}{1/(C_0 R_e) + \psi_a - (\psi_a - 1/(C_0 R_e))\exp(-\eta^2/a^2)}\right]^{a^2/2} & \text{clean surface,} \\ \exp(-\eta^2/2)\left[\dfrac{1/(C_0 R_e)}{1/(C_0 R_e) + \psi_a - \psi_a \exp(-\eta^2/a^2)}\right]^{a^2/2} & \text{contaminated surface.} \end{cases} \tag{4.13}$$

4.2. *Comparison between theoretical similarity solution and numerical results*

We compare the similarity solution in § 4.1 to results of our direct numerical simulations. The comparison is performed as follows. The value of velocity deficit U_d, the bulk eddy viscosity ψ_a, and the surface eddy viscosity ψ_0 are obtained directly from numerical results based on their definitions. The shear extent b is determined by matching $f(\eta)$ in (4.13) with the numerical value at the depth $\eta = -1$, and the value of a is obtained by a least-squares best fit of (4.12).

The obtained parameters are given in tables 2 and 3. Figures 17, 18 and 19 compare profiles of eddy viscosity mean velocity and mean shear, respectively. In general, the numerical data agree with theoretical solutions with remarkable accuracy. Different cases with different Reynolds numbers are all represented well by the analytic solution. In each case, the DNS data at different times, which have different physical values, all collapse onto the curve predicted by the similarity solution.

	Re	C_0	Q	ψ_a	ψ_0	$C_0 Re \psi_0$	a	$a\sqrt{C_0 Re \psi_a}$	ϵ	$\sqrt{C_0 Re}\,\epsilon/a$
(a)	700	1.04	−0.65	0.0228	1.40×10^{-3}	1.05	0.305	1.24	0.115	10.2
	1000	1.02	−0.14	0.0229	0.98×10^{-3}	1.00	0.251	1.21	0.078	9.9
	1400	1.01	−0.03	0.0224	0.78×10^{-3}	1.10	0.215	1.21	0.058	10.1
(b)	700	1.18	−1.09	0.0230	0.37×10^{-5}	n/a	0.418	1.82	0.091	6.3
	1000	1.14	−0.54	0.0232	0.28×10^{-5}	n/a	0.356	1.83	0.067	6.4
	1400	1.14	−0.42	0.0237	0.22×10^{-5}	n/a	0.308	1.89	0.049	6.4

TABLE 3. Values of C_0, Q, ψ_a, ψ_0, a and ϵ, for the clean- ($Ma = 0$) and contaminated-surface ($Ma = 0.1$) cases at different Re. (a) $Ma = 0$, (b) $Ma = 0.1$.

Table 2 gives the variation with time of the mean shear extent b, the mean velocity deficit U_d, and the product $C_0 = U_d b$ for the contaminated-surface case $Ma = 0.1$. The clean-surface data ($Ma = 0$) is given by P2 and will not be repeated here. We find that the variation of b and U_d agrees well with the predictions (4.9) and (4.10) to within 2% (results not shown here). Table 2 also shows that $C_0 = U_d b$ remains strictly constant to within 1%. The constant value of C_0 in time shows the momentum conservation in our solutions. The deviation of C_0 from the unit value is due to the fact that we chose for normalization the initial profile (2.10), when the truly physical free-surface turbulence has not been developed. Indeed, normalization based on U_d and b of the similarity solution will be more physical.

Figure 17 compares the profiles of the eddy viscosity between the analytic expression (4.12) and the DNS data. The contaminated-surface case with different Reynolds numbers of $Re = 700$, 1000, 1400 are shown. For comparison, we also plot the clean-surface case with $Re = 700$. The eddy viscosity variation as a function of the distance from the surface is approximated well by the Gaussian profile. For a specific Reynolds number, despite the fact that the surface-layer thickness changes as time evolves, the normalization using the similarity variable makes all the data collapse onto a single curve. Comparison between figures 17(a) and 17(b) shows that the free-surface outer layer (the region over which the eddy viscosity decreases) is thicker in the contaminated-surface case than that in the clean-surface case. Comparison among figures 17(b), 17(c) and 17(d) shows that the outer layer becomes thinner as the Reynolds number increases. This can be seen more clearly from the values of a given in table 3.

Figure 17 shows that in the bulk flow, the eddy viscosity is the same for all cases. This can be seen more clearly from the values of ψ_a given in table 3. This is expected because the Reynolds number and the free-surface condition do not affect the turbulent diffusion process in the bulk flow far below the surface. At the free surface, however, the eddy viscosity is very much affected by the presence of surfactants. At the clean surface, the fact that $C_0 Re \psi_0$ remains a unit value (table 3) means that the eddy viscosity has a value of molecular viscosity. We can also see from table 3 that the value of eddy viscosity at the contaminated surface is much smaller (by two orders of magnitude) than that at a clean surface.

The profiles of the mean velocity and mean shear are compared in figures 18 and 19, respectively. We can see that the similarity solution agrees with the DNS results with remarkable accuracy. Of significant importance, the similarity solution, which is a function of the Reynolds number, is applicable to the DNS cases with different Re. For each case, despite the fact the physical values of the mean velocity and mean shear change in time (figure 2), the normalization again makes all the data points collapse

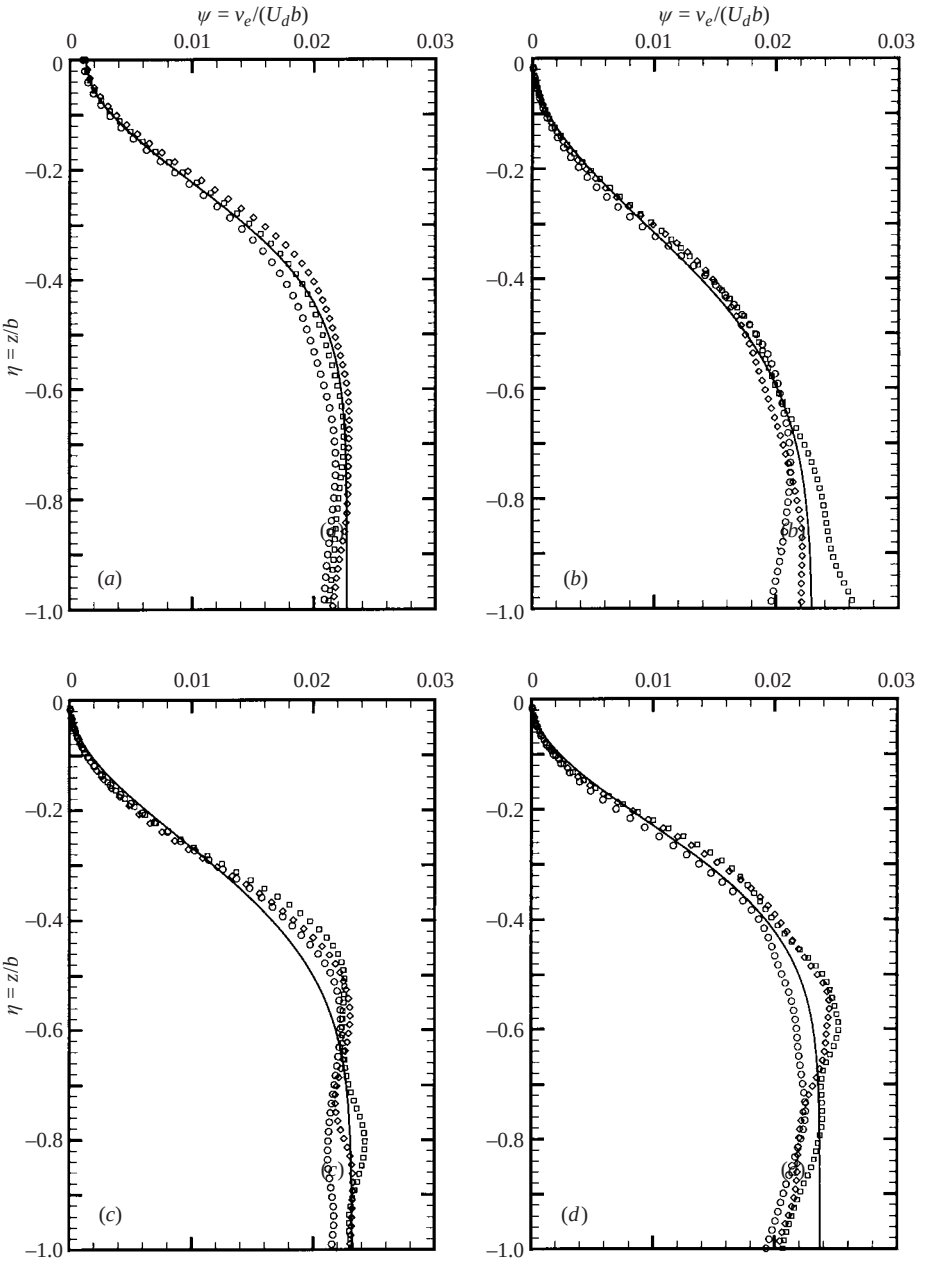

FIGURE 17. Comparison of the eddy viscosity profile between the similarity solution (————) and the DNS results for: (*a*) the clean-surface case ($Ma = 0$), $Re = 700$; ○, $t = 60$; □, $t = 70$; ◇, $t = 80$; and the contaminated-surface cases ($Ma = 0.1$) with (*b*) $Re = 700$, (*c*) $Re = 1000$ and (*d*) $Re = 1400$; ∘, $t = 70$; □, $t = 80$; ◇, $t = 90$.

onto the theoretical curve. Notably, the similarity solution accurately captures the rapid variation of the mean shear near the free surface.

Comparison between the clean- and contaminated-surface cases in figure 19 shows that surface contamination makes the near-surface peak of the mean shear about twice as large as that in the clean-surface case. Comparison of figures 19(*b*), 19(*c*) and

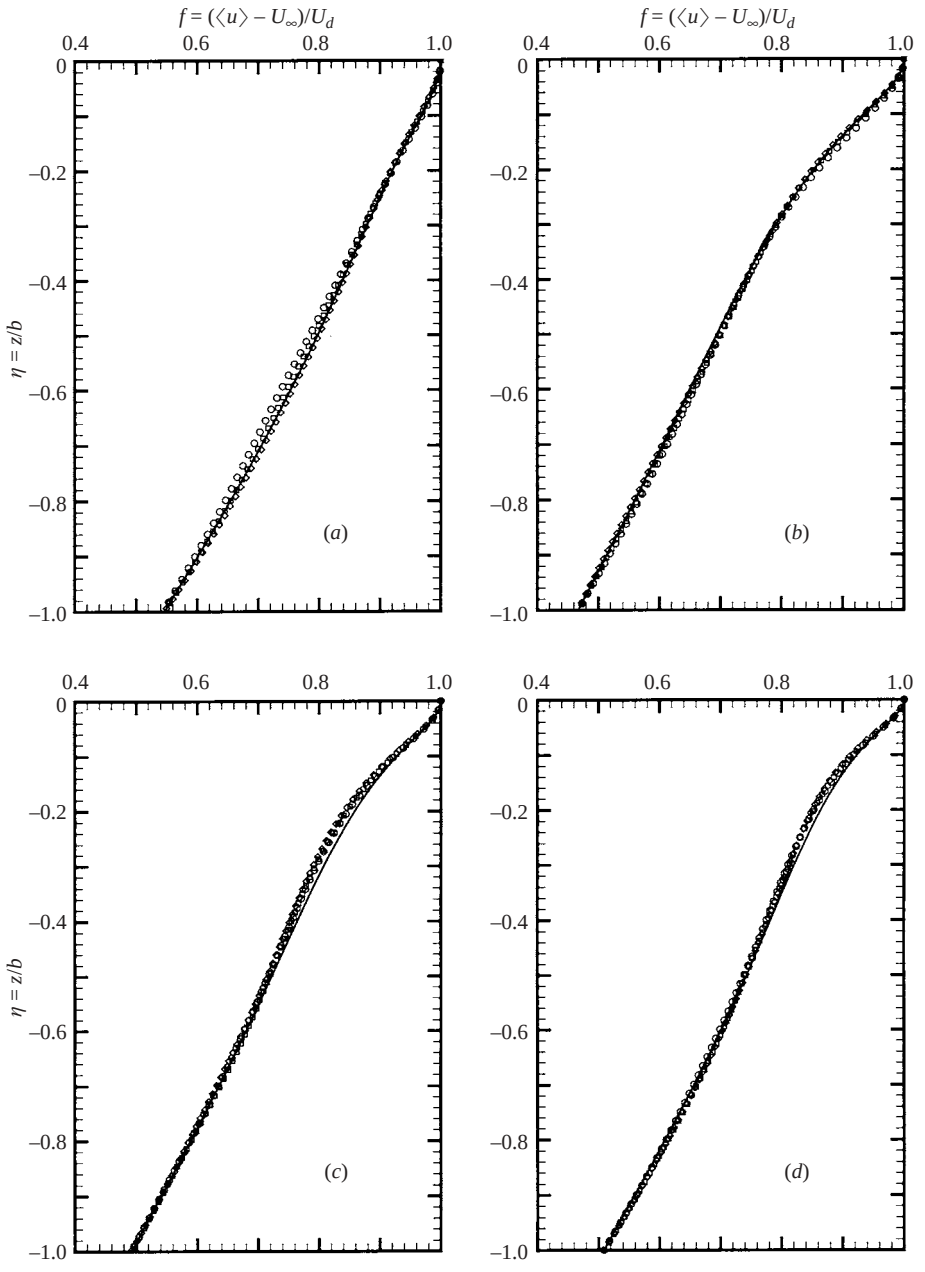

FIGURE 18. Comparison of the mean velocity profile between the similarity solution (————) and the DNS results as for figure 17.

19(*d*) further shows the decreasing of surface-layer thickness as the Reynolds number increases. The underlying mechanisms for these phenomena are discussed in the next section.

4.3. *The scaling laws of the free-surface boundary layer*

The analytic solution (4.11) specifies the dependence of the mean flow profile on the variation of eddy viscosity. It forms a basis for the quantitative description of

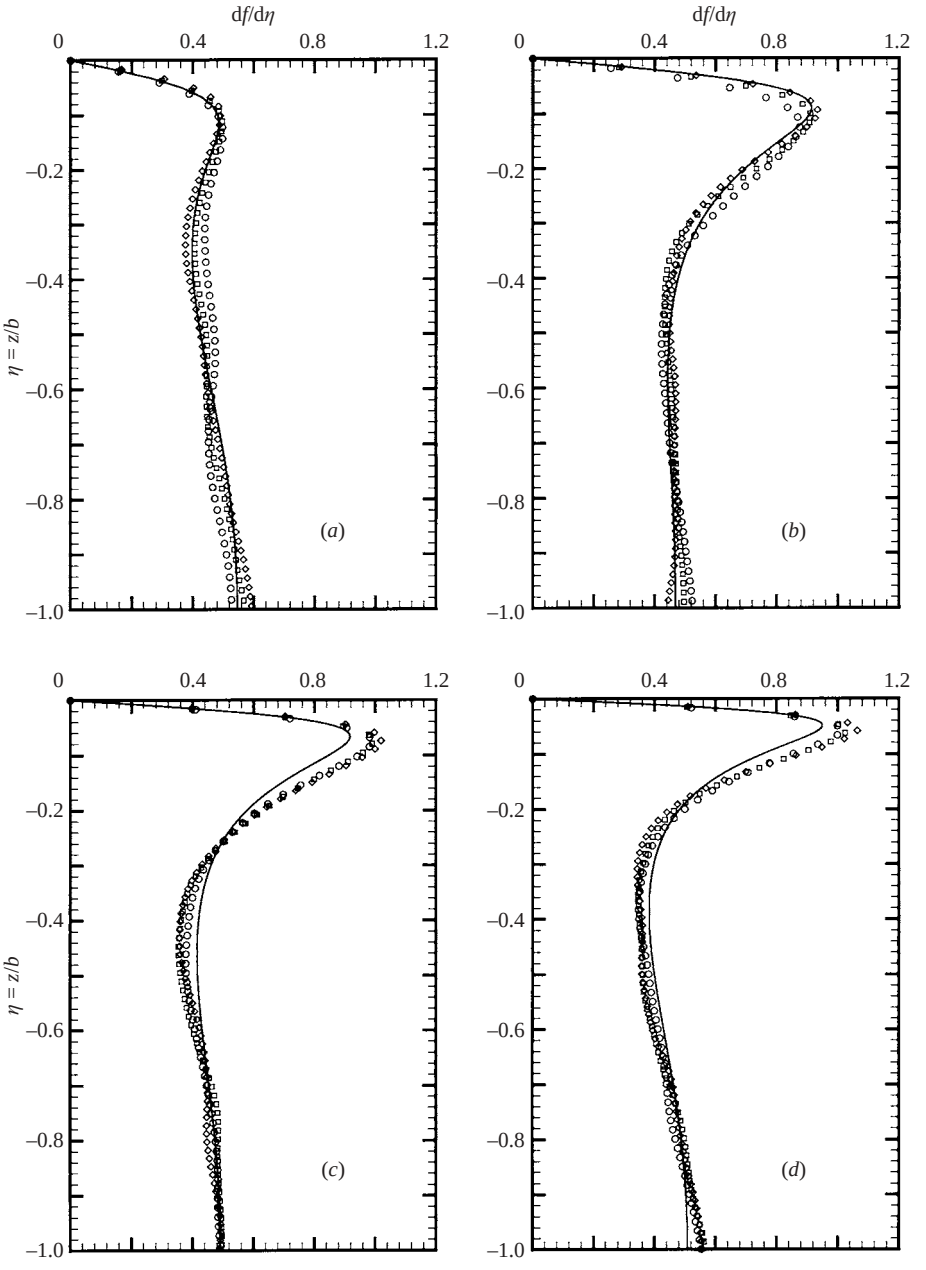

FIGURE 19. Comparison of the mean shear profile between the similarity solution (————) and the DNS results as for figure 17.

the free-surface boundary-layer structure. Similar to P2, we define the surface outer layer as the region where the eddy viscosity decreases and the mean shear increases. The surface inner layer is defined as the region where the eddy viscosity becomes comparable to the molecular viscosity and the mean shear decreases to the zero surface-value.

In principle, we can use the small-argument approximation of (4.11) to obtain the thickness of the outer and inner layers. On the other hand, our DNS results show that the eddy-viscosity profile can be approximated by a Gaussian profile and as a result, the integration in (4.11) can be obtained explicitly in (4.13). This analytic and explicit expression greatly facilitates our analysis.

We first consider the inner-layer thickness. Using a small-η expansion, we can write (4.13) as

$$f(\eta) \approx \begin{cases} (1-\eta^2/2)\left[\dfrac{2/(C_0R_e)}{2/(C_0R_e)+\psi_a\eta^2/a^2}\right]^{a^2/2} & \text{clean surface,} \\ (1-\eta^2/2)\left[\dfrac{1/(C_0R_e)}{1/(C_0R_e)+\psi_a\eta^2/a^2}\right]^{a^2/2} & \text{contaminated surface.} \end{cases} \tag{4.14}$$

Let ϵ be the thickness of the inner layer (normalized by b). Using a dominant balance argument for the expression in the denominator on the right-hand side of (4.14), we obtain

$$\epsilon \sim \begin{cases} \sqrt{2}a\psi_a^{-1/2}C_0^{-1/2}Re^{-1/2} & \text{clean surface,} \\ a\psi_a^{-1/2}C_0^{-1/2}Re^{-1/2} & \text{contaminated surface.} \end{cases} \tag{4.15}$$

The above equation can also be obtained by searching for the location where the maximum value of the mean shear occurs based on the profile (4.13).

Equation (4.15) shows that the ratio of the inner-layer thickness to the outer-layer thickness is proportional to $Re^{-1/2}$. This ratio in the clean-surface case is $\sqrt{2}$ times larger than that in the contaminated-surface case. These predictions are directly confirmed by our simulation results shown in table 3, as indicated by the numerical value of $\sqrt{C_0Re}\,\epsilon/a$. In table 3, the numerical value of ϵ is defined based on the location where the mean shear reaches its maximum value.

We next consider the outer-layer thickness. Consider the mean shear profile f' which is the first derivative of (4.14). We find that the maximum shear $s_m \equiv f'|_{max}$, which occurs at the location given by (4.15), has the value

$$s_m \sim \begin{cases} a\,(C_0R_e\psi_a)^{1/2}/(2\sqrt{2}) & \text{clean surface,} \\ a\,(C_0R_e\psi_a)^{1/2}/2 & \text{contaminated surface.} \end{cases} \tag{4.16}$$

Given that s_m remains bounded as Re increases (cf. figure 19), a is given by

$$a \sim (C_0R_e\psi_a)^{-1/2}. \tag{4.17}$$

Therefore, the ratio of the outer-layer thickness to the mean shear extent (note that a is normalized by b) is also proportional to $Re^{-1/2}$. This prediction is again confirmed by the DNS data given in table 3, as indicated by the numerical values of $a\sqrt{C_0Re\psi_a}$. Table 3 also shows that this ratio is larger in the contaminated-surface case than in the clean-surface case. In other words, the outer layer is thicker below a surfactant-contaminated surface. This difference together with the different formulation of the maximum shear (equation (4.16), which is caused by a different value of eddy viscosity at the free surface) make the maximum shear in the contaminated-surface case about twice as large as that in the clean-surface case (figure 19).

To summarize, our theoretical analysis and numerical simulation obtain consistent scaling relationships for the free-surface boundary-layer structure. Both the ratio of outer-layer thickness to the mean shear extent and the ratio of inner-layer thickness to the outer-layer thickness scale as the Reynolds number to the power of minus

a half. The surface condition affects the factors of proportionality. The first ratio is larger in the contaminated-surface case than in the clean-surface case, while the second ratio is smaller in the contaminated-surface case. In other words, for the same mean shear extent and at the same Reynolds numbers, the outer layer is thicker near a surfactant-contaminated surface than near a clean surface, while the inner layers have about the same thickness.

4.4. *Discussion*

The proceeding sections elucidate the free-surface outer and inner layers, which can be characterized by the increasing and decreasing of the mean shear as the free surface is approached. Comparison between the surfactant-contaminated surface and the clean surface results shows that: (i) the outer layer is thicker near a contaminated surface; (ii) the surface value of eddy viscosity equals molecular viscosity at the clean surface, but is negligibly small at a contaminated surface. From table 3, we see that the first factor contributes to a 50% increase in the peak shear rate while the second factor contributes another 40%.

Both these factors can be understood through the surface divergence $(\partial u/\partial x + \partial v/\partial y)|_{z=0} = -(\partial w/\partial z)|_{z=0}$. As shown in § 3.1, surface elasticity caused by the surfactant prohibits surface upwelling/downwelling flow (i.e. the splat/anti-splat motion). As a result, $(\partial w/\partial z)|_{z=0}$ is much smaller at a contaminated surface. Consider the vertical velocity near a free surface. Taylor expansion gives

$$w(z) = w|_{z=0} + \left.\frac{\partial w}{\partial z}\right|_{z=0} z + O(z^2). \tag{4.18}$$

Since w' is responsible for turbulent diffusion in the vertical direction, and since the outer layer is the region where turbulent diffusion is reduced owing to the presence of the surface, (4.18) shows that a contaminated surface affects an outer layer more deeply than a clean surface does.

The second factor, the difference in the surface value of eddy viscosity, can be explained by rewriting (4.4) as

$$\nu_e|_{z=0} = \frac{\langle -w'\partial u'/\partial z - u'\partial w'/\partial z\rangle|_{z=0}}{\partial^2\langle u\rangle/\partial z^2|_{z=0}}. \tag{4.19}$$

In the numerator of (4.19), the second term dominates because of the small value of w in the first term. As a result, the surface value of eddy viscosity is directly related to surface divergence $(\partial w/\partial z)|_{z=0} = -(\partial u/\partial x + \partial v/\partial y)|_{z=0}$, and is much smaller in the presence of surfactant.

Finally, we remark that although the physical parameters we choose for this problem are not unrealistic (see § 2.2), the choice of a surface free-shear flow as our canonical problem makes it more difficult to find experimental data for direct comparison. From theoretical and computational points of view, the study of free shear flows has advantages, such as the existence of the similarity solution for the mean flow which offers a clear view of the boundary layer at the free surface. Most experiments however have been performed on pressure/gravity-driven open-channel flows (e.g. Nezu & Nakagawa 1993).

In order to test some of our basic findings obtained from this study, we have obtained limited results (using the implicit numerical scheme) for open-channel flows with clean and contaminated surfaces. The essential features we find for the free-shear flow are all also observed here. Figure 20 shows representative results for the case of a pressure-driven open-channel flow. In figure 20(*a*), mean velocity profiles are compared

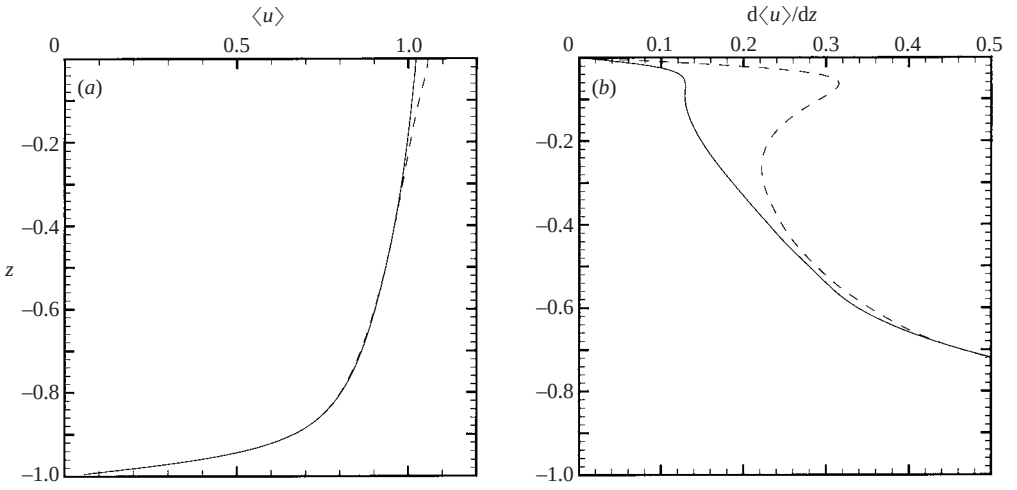

FIGURE 20. Profiles of (*a*) mean velocity $\langle u \rangle$, and (*b*) mean shear $d\langle u \rangle/dz$ in open-channel flows. ————, clean surface; – – – –, contaminated surface.

for the clean and contaminated surface cases. Higher values of the mean velocity are observed near the surfactant surface, similar to the results shown in figure 2 for time-evolving free-shear flows. The surfactant effects are more distinct in the mean shear profile (figure 20*b*). For the clean surface case, the local minimum and maximum of the mean shear is weaker compared to those in free-shear flows (cf. figure 16*a*) because of the presence of streamwise body forces (the shear profile becomes a 'terrace' between the lower boundaries of the outer and inner layers). The presence of surfactants, however, causes drastic variation in the mean shear near the free surface, which can be used to quantify the surface boundary layers. For the simulation shown in figure 20, the Reynolds number based on the surface mean velocity and the channel depth is 3700, which is well within the range of laboratory experiments (cf. table 1 in Kumar, Gupta & Banerjee 1998); the Marangoni number for the surfactant is 0.1, also quite feasible for experiments, as discussed in § 2.2. Unfortunately, experimental surfactant results here are, to our knowledge, still unavailable; and we hope that results like those in figure 20 might provide an impetus for such measurements.

5. Conclusions

In this paper, we study the effect of surfactants on the boundary layer at a free surface. The hydrodynamics of the flow studied are dictated by the Reynolds number and the surfactant dynamics by the Marangoni number (the Froude number is allowed to vary, but kept small while the Péclet and Weber numbers are kept constant).

The turbulent boundary layers near either a contaminated or clean (cf. P1, P2) free surface share the following general features. The kinematic constraint of the surface on the fluid vertical motions creates an outer layer within which the velocity is anisotropic. At low Froude numbers, horizontal velocity fluctuations far exceed the vertical velocity fluctuations and the anisotropy is maximum at the free surface. The flow inside the outer layer, however, is not two-dimensional because of the existence of upwellings and downwellings. Inside the outer layer and in the vicinity of the surface, there exists a much thinner inner layer where the dynamic surface conditions governing

the cross-surface stress balance are felt. Within the inner layer, quantities such as vorticity and strain rate are highly anisotropic. This two-layer structure is distinct in the profile of the mean shear. As the surface is approached, the mean shear rises over the outer layer and drops sharply to zero over the inner layer. The boundaries of the two layers can be defined precisely as the locations where the magnitude of the shear exhibits a local minimum (outer layer) and maximum (inner layer).

The presence of surfactants, however, has a significant effect on important aspects of the near-surface flow even for very small values of the Marangoni number. One effect is that surfactant elasticity greatly reduces the flow divergence at the surface. This is the result of a closed-loop effect where surface divergent/convergent motions resulting from the up-/downwelling cause a decrease/increase in the surfactant concentration, which in turn creates gradients in the surface tension to counter the fluid motion. The picture is further clarified by consideration of the underlying vortical structures in terms of the generation of Marangoni vorticity by hairpin vortices associated with splats. As expected, surface contamination also reduces the near-surface turbulence fluctuations. We are able to elucidate the mechanism through a quantification of the terms in the turbulent kinetic energy equation. Near the surface, surface elasticity increases dissipation and viscous diffusion, but reduces turbulence production, transport and inter-component redistribution compared to the clean case. In terms of magnitude and sensitivity to Ma, however, we find that surface divergence, rather than turbulence intensities, is clearly a better indicator of surface contamination. The decrease of surface divergence and the associated reduction in upwelling and downwelling also has significant implications to near-surface turbulent transport. One example of such processes is the surface renewal associated with gas transfer across the air–water interface (Shen 2001).

As mentioned above, the maximum and minimum of the mean shear profile offer quantitative indicators of the surface multi-layer structure. These extrema are much more distinct when the surface is contaminated by surfactants. To understand the underlying mechanism and to obtain the scaling laws for the surface-layer thickness, we develop an analytic similarity solution for the mean flow. The theoretical predictions of the mean flow profile agree with our direct numerical simulations with remarkable accuracy. The similarity solution predicts that the thickness of the outer layer is proportional to the depth of the mean shear flow, while the thickness of the inner layer is proportional to that of the outer layer. In both cases the thickness ratios scale as $Re^{-1/2}$. These scaling laws are also confirmed by our numerical results. By taking into account the reduction effect of surfactants on surface divergence, the similarity solution also predicts the observation in simulations that compared to the clean-surface case, the outer layer in the presence of surfactants is thicker while the inner layer has approximately the same thickness. This analytic similarity solution provides theoretical insights for the underlying mechanisms and establishes a basis for the development of physics-based turbulence models.

We have made (mostly) qualitative/indirect comparisons to physical measurements where they are available. Laboratory measurements that can provide direct quantitative comparisons to what we find are, however, absent and would clearly be most desirable.

This research was financially supported by the Office of Naval Research. Most of the computations were performed at the Naval Oceanographic Office (NAVOCEANO) Major Shared Resource Center (MSRC) on IBM-SP3 as part of a DoD Challenge Project under the DoD HPC Modernization Program.

REFERENCES

Ananthakrishnan, P. & Yeung, R. W. 1994 Nonlinear interaction of a vortex pair with clean and surfactant-covered free surfaces. *Wave Motion* **19**, 343–365.

Anthony, D. G., Hirsa, A. & Willmarth, W. W. 1991 On the interaction of a submerged turbulent jet with a clean or contaminated free surface. *Phys. Fluids* A **3**, 245–247.

Barger, W. R. 1991 A review of experimental observations and remaining questions concerning formation, persistence, and disappearance of sea slicks. *NRL Rep. 9313*.

Batchelor, G. K. 1967 *An Introduction to Fluid Dynamics*. Cambridge University Press.

Bernal, L. P., Hirsa, A., Kwon, J. T. & Willmarth, W. W. 1989 On the interaction of vortex rings and pairs with a free surface active agent. *Phys. Fluids* A **1**, 2001–2004.

Blackwelder, R. F. & Kaplan, R. E. 1976 On the wall structure of the turbulent boundary layer. *J. Fluid Mech.* **76**, 89–112.

Broglia, R., Pascarelli, A. & Piomelli, U. 2003 Large-eddy simulations of ducks with a free surface. *J. Fluid Mech.* **484**, 223–253.

Calmet, I. & Magnaudet, J. 2003 Statistical structure of high-Reynolds-number turbulence close to the free surface of an open-channel flow. *J. Fluid Mech.* **474**, 355–378.

Edwards, D. A., Brenner, H. & Wasan, D. T. 1991 *Interfacial Transport Processes and Rheology*. Butterworth–Heinemann.

Flack, K. A., Saylor, J. R. & Smith, G. B. 2001 Near-surface turbulence for evaporative convection at an air/water interface. *Phys. Fluids* **13**, 3338–3345.

Frew, N. M. 1997 The role of organic films in air–sea gas exchange. *The Sea Surface and Global Change* (ed. P. S. Liss & R. A. Duce), pp. 121–172. Cambridge University Press.

Frew, N. M. & Nelson, R. K. 1992 Scaling of marine microlayer film surface pressure–area isotherms using chemical attributes. *J. Geophy. Res.* **97** C4, 5291–5300.

Gharib, M. & Weigand, A. 1996 Experimental studies of vortex disconnection and connection at a free surface. *J. Fluid Mech.* **321**, 59–86.

Handler, R. A., Swean, T. F. Jr., Leighton, R. I. & Swearingen J. D. 1993 Length scales and the energy balance for turbulence near a free surface. *AIAA J.* **31**, 1998–2007.

Harber, C. D. & Gulliver, J. S. 1992 Surface-films in laboratory flumes. *J. Hydraul. Res.* **30**, 801–815.

Hartel, C., Kleiser, L., Unger, F. & Friedrich, R. 1994 Subgrid-scale energy transfer in the near-wall region of turbulent flows. *Phys. Fluids* **6**, 3130–3143.

Hinze, J. O. 1975 *Turbulence*. McGraw-Hill, New York.

Hirsa, A., Lopez, J. M. & Miraghaie, R. 2001 Measurement and computation of hydrodynamic coupling at an air/water interface with an insoluble monolayer. *J. Fluid Mech.* **443**, 271–292.

Hirsa, A. & Willmarth W. W. 1994 Measurement of vortex pair interaction with a clean or contaminated free surface. *J. Fluid Mech.* **259**, 25–45.

Hunter, K. A. 1997 Chemistry of the sea-surface microlayer. *The Sea Surface and Global Change* (ed. P. S. Liss & R. A. Duce), pp. 287–319. Cambridge University Press.

Jähne, B. & Haussecker, H. 1998 Air–water gas exchange. *Annu. Rev. Fluid. Mech.* **30**, 443–68.

Kim, J. 1983 On the structure of wall-bounded turbulent flows, *Phys. Fluids* **26**, 2088–2097.

Kim, J. & Moin, P. 1985 Application of a fractional-step method to impressible Navier–Stokes equations. *J. Comput. Phys.* **59**, 308–323.

Kumar, S., Gupta, R. & Banerjee, S. 1998 An experimental investigation of the characteristics of free-surface turbulence in channel flow. *Phys. Fluids* **10**, 437–456.

Longuet-Higgins, M. S. 1998 Vorticity and curvature at a free surface. *J. Fluid Mech.* **356**, 149–153.

Lopez, J. M. & Hirsa, A. H. 2000 Surfactant-influenced gas–liquid interfaces: nonlinear equation of state and finite surface viscosities. *J. Colloid Interface Sci.* **229**, 575–583.

McKenna, S. P. 2000 Free-surface turbulence and air–water gas exchange. *PhD thesis*, MIT/WHOI Joint Program.

Mansour, N. N., Kim, J. & Moin, P. 1988 Reynolds-stress and dissipation-rate budgets in a turbulent channel flow. *J. Fluid Mech.* **194**, 15–44.

Mattingly, G. E. & Criminale, W. O. 1972 The stability of an incompressible two-dimensional wake. *J. Fluid Mech.* **51**, 233–272.

Nagaosa, R. 1999 Direct numerical simulation of vortex structures and turbulent scalar transfer across a free surface in a fully developed turbulence. *Phys. Fluids* **11**, 1581–1595.

NEZU, I. & NAKAGAWA, H. 1993 *Turbulence in Open-Channel Flows*. Rotterdam.

PEROT, B. & MOIN, P. 1995 Shear-free turbulent boundary layers. Part 1. Physical insights into near-wall turbulence. *J. Fluid Mech.* **295**, 199–227.

PIOMELLI, U., YU, Y. & ADRIAN, R. J. 1996 Subgrid-scale energy transfer and near-wall turbulence structure. *Phys. Fluids* **8**, 215–224.

SARPKAYA, T. 1996 Vorticity, free surface, and surfactants. *Annu. Rev. Fluid. Mech.* **28**, 83–128.

SCOTT, J. C. 1982 Flow beneath a stagnant film on water: the Reynolds ridge. *J. Fluid Mech.* **116**, 283–296.

SCRIVEN, L. E. 1960 Dynamics of a fluid interface. *Chem. Engng Sci.* **12**, 98–108.

SHEN, L. 2001 Structures, statistics and mechanics of low Froude number free-surface turbulence – a simulation-based study. *PhD thesis*, Dept. Ocean Engng, MIT.

SHEN, L., TRIANTAFYLLOU, G. S. & Yue, D. K. P. 2000 Turbulent diffusion near a free surface. *J. Fluid Mech.* **407**, 145–166. (Referred to herein as P2.)

SHEN, L., ZHANG, X., Yue, D. K. P. & TRIANTAFYLLOU, G. S. 1999 The surface layer for free-surface turbulent flows. *J. Fluid Mech.* **386**, 167–212. (Referred to herein as P1.)

SMITH, G. B., VOLINO, R. J., Handler, R. A. & LEIGHTON, R. I. 2001 The thermal signature of a vortex pair impacting a free surface. *J. Fluid Mech.* **444**, 49–78.

TRYGGVASON, G., ABDOLLAHI-ALIBEIK, J., WILLMARTH, W. W. & HIRSA, A. 1992 Collision of a vortex pair with a contaminated free surface. *Phys. Fluids* **4**, 1215–1229.

TSAI, W. T. 1996 Impact of a surfactant on a turbulent shear layer under the air–sea interface. *J. Geophys. Res.* **101** C12, 28 577–28 568.

TSAI, W. T. & YUE, D. K. P. 1995 Effects of soluble and insoluble surfactant on laminar interactions of vortical flows with a free surface. *J. Fluid Mech.* **289**, 315–349.

WALKER, D. T., LEIGHTON, R. I. & GARZA-RIOS, L. O. 1996 Shear-free turbulence near a flat free surface. *J. Fluid Mech.* **320**, 19–51.

WANG, H. T. & LEIGHTON, R. I. 1990 Direct calculation of the interaction between subsurface vortices and surface contaminants. *Proc. 19th Intl Conf. Offshore Mech. Arctic Engng*, pp. 271–277.

WARNCKE, A., GHARIB, M. & ROESGEN, T. 1996 Flow measurements near a Reynolds ridge. *J. Fluid Engng* **118**, 621–624.

WILLERT, C. E. & GHARIB, M. 1997 The interaction of spatially modulated vortex pairs with free surfaces. *J. Fluid Mech.* **345**, 227–250.

ZHANG, X. 2001 Surfactant effects on the interaction of a three dimensional vortex pair with a free surface. *PhD thesis Part I*, Dept. Ocean Engng, MIT.